# Trackable and highly fluorescent nanocellulose-based printable bio-resins for image-guided tissue regeneration

Sayan Deb Dutta [a,b], Tejal V. Patil [a,c], Keya Ganguly [a], Aayushi Randhawa [a,c], Rumi Acharya [a,c], Md Moniruzzaman [d], Ki-Taek Lim [a,b,c,*]

[a] *Department of Biosystems Engineering, Kangwon National University, Chuncheon 24341, Gangwon-do, Republic of Korea*
[b] *Institue of Forest Science, Department of Biosystems Engineering, Kangwon National University, Chuncheon 24341, Gangwon-do, Republic of Korea*
[c] *Interdisciplinary Program in Smart Agriculture, Kangwon National University, Chuncheon 24341, Gangwon-do, Republic of Korea*
[d] *Department of Chemical and Biological Engineering, Gachon University, Seongnam, Gyeonggi-do 13120, Republic of Korea*

ARTICLE INFO

ABSTRACT

Dynamic tracking of cell migration during tissue regeneration remains challenging owing to imaging techniques that require sophisticated devices, are often lethal to healthy tissues. Herein, we developed a 3D printable non-invasive polymeric hydrogel based on 2,2,6,6-(tetramethylpiperidin-1-yl) oxyl (TEMPO)-oxidized nanocellulose (T-CNCs) and carbon dots (CDs) for the dynamic tracking of cells. The as-prepared T-CNC@CDs were used to fabricate a liquid bio-resin containing gelatin methacryloyl (GelMA) and polyethylene glycol diacrylate (GPCD) for digital light processing (DLP) bioprinting. The shear-thinning properties of the GPCD bio-resin were further improved by the addition of T-CNC@CDs, allowing high-resolution 3D printing and bioprinting of human cells with higher cytocompatibility (viability ~95 %). The elastic modulus of the printed GPCD hydrogel was found to be ~13 ± 4.2 kPa, which is ideal for soft tissue engineering. The as-fabricated hydrogel scaffold exhibited tunable structural color property owing to the addition of T-CNC@CDs. Owing to the unique fluorescent property of T-CNC@CDs, the human skin cells could be tracked within the GPCD hydrogel up to 30 days post-printing. Therefore, we anticipate that GPCD bio-resin can be used for 3D bioprinting with high structural stability, dynamic tractability, and tunable mechanical stiffness for image-guided tissue regeneration.

## 1. Introduction

Despite significant progress in image-guided therapy, real-time monitoring of damaged or regenerated tissue remains challenging owing to the lack of clinically relevant tabletop imaging systems (Choi & Kim, 2020; Shin et al., 2017). To date, minimally invasive procedures for tracking tumor, wound, or surgical implants rely on conventional imaging technologies, such as X-ray fluoroscopy, computed tomography (CT), ultrasound (US), or magnetic resonance (MR)-based imaging; these techniques require sophisticated instrumentation and high-power electrical devices, and are therefore not a cost-effective strategy (Choi & Kim, 2020; Park et al., 2021). Moreover, MR or radiotherapy-based imaging of soft tissues or organs requires additional contrasting agents that can harm the human body to some extent. Furthermore, soft biomedical implants lack a suitable tracking system; therefore, tissue regeneration after surgical intervention often fails to demonstrate the regeneration capabilities of pre-clinical polymeric hydrogels (Park et al.,

2021). In contrast, the fluorescent imaging technique has gained enormous attention in medical diagnostics and surgery owing to its non-invasive nature, superior resolution, transparent visualization, and dynamic tracking of the recapitulated tissue (Hyun et al., 2015). Notably, near-infrared (NIR) fluorescence imaging is often beneficial for imaging biological tissues with super-high resolution. Based on the above facts, biomedical implants with a self-tracking system are highly desirable for image-guided tissue regeneration studies.

3D additive manufacturing (AM) allows rapid prototyping of complex biological architectures after translating the medical anatomical code (CT scan data) into a printable code (CAD model). Among the various techniques, photopolymerization-based AM technology uses a light source (*e.g.*, ultraviolet, visible, or near-infrared) to crosslink photopolymers *via* free-radical polymerization (Maturi et al., 2020). Stereolithography (SLA), digital light processing (DLP), and two-photon lithography (TPL) are the commonly used light-assisted 3D printing techniques for constructing various structures especially useful in

---

microelectromechanical systems/nanoelectromechanical systems (MEMS/NEMS) (Cesewski et al., 2018; Dai et al., 2021; Sanchez Noriega et al., 2021), optoelectronics (Camposeo et al., 2019), tissue engineering (Bose et al., 2020; Chan et al., 2021; Wei et al., 2022), nanophotonics (Boyle et al., 2017), and optical tweezing (Chizari et al., 2019) among others. DLP-based 3D printing is a vat polymerization-based printing technique frequently used in the biomedical field to develop complex tissue and organ structures (Hong et al., 2020). DLP bioprinter uses a resin vat and UV projection digital mirror device (DMD), which help to cure the photopolymer resin layer-by-layer to generate high-resolution 3D structures (Kim et al., 2018; Zhu et al., 2016). To date, most photocurable resins have been chemically-synthesized or are epoxy-based, and they are slightly toxic to the human cells. However, a few biocompatible polymer resins, such as carboxymethyl cellulose (Melilli et al., 2020), silk fibroin (Hong et al., 2020), poly(glycerol-*co*-propanediyl) itaconate-*co*-vanillate (Maturi et al., 2020), soybean oil (Skliutas et al., 2020), and gelatin (Ye et al., 2020) are widely used for DLP printing. Printable resins are reinforced with various nanofillers to improve viscoelasticity, thermal stability, mechanical properties, and printability (Drury & Mooney, 2003). Most printable bio-resins lack fluorescent properties, and therefore, the tracking ability during cell culture. Furthermore, the commercial fluorescent probes used for hydrogel staining were often dissolved in organic solvents (*e.g.*, dimethyl sulfoxide), which also displayed slight cytotoxicity to the encapsulated cells (Pal et al., 2012; Simsek Öz et al., 2012). Maturi et al. reported using a chemically modified bio-based phosphorescence resin composed of itaconic acid, vanillic acid, and propanediol for skin tissue engineering (Maturi et al., 2020). Similarly, GFP-tagged methacrylated silk fibroin and CdSe quantum dots reinforced bio-resins have also been used to encapsulate fibroblast cells (hDFs) (Jaiswal et al., 2021; Lee et al., 2022). Bae et al. used nanoclay and cellulose nanocrystals (CNCs) to reinforce DC-36 resins with improved DLP printing properties but lacking fluorescent properties (Bae & Kim, 2021). In another study, cellulose nanofibrils (CNFs) and graphene oxide (GO) were used to reinforce the polyurethane (PU) resins (Mohan et al., 2019). Nanocellulose (*e.g.*, CNCs and CNFs) has long been utilized as a bio-based nanofiller for tuning printability and mechanical properties with excellent biocompatibility (Luo et al., 2019). The surface chemistry of nanocellulose can be tuned *via* grafting with various chemical moieties to improve the biological features, such as cell adhesion and differentiation (Mujtaba et al., 2023), and also control the viscosity of the hydrogel inks during 3D printing in a concentration-dependent manner (Heidarian & Kouzani, 2023; Patel et al., 2023). Despite several advancements in nanocellulose research, the use of fluorescent nanocellulose for tissue engineering and bioprinting is not well-explored.

CNCs have been used extensively as reinforcing agents for extrusion-based 3D printing applications (Xu et al., 2018). For instance, higher concentrations of CNCs may contribute to the higher mechanical strength and increase the shear-thinning/thickening and stress-yielding properties *via* increasing visco-elasticity in the polymer matrix during 3D printing (Fourmann et al., 2021; Sultan et al., 2017; Sultan et al., 2019). Low concentration CNC-formulations had minimal effect on building high-resolution constructs by extrusion-based printing owing to the little reinforcement effect. In this context, the low-concentration CNC-formulation could be used as a resin for DLP printing, which uses a layer-by-layer curing method in the liquid state. A recent study describes using CNF-immobilized polyborosilazane (CNF/PBSN) resins for electromagnetic shielding applications (Liu et al., 2022).

The purpose of this research is to develop new and fully bio-based resin formulations for DLP printing using biocompatible polymers and fluorescent TEMPO-CNCs (T-CNCs) at extremely low concentrations. To the best of our knowledge, the formulation of fluorescent nanocellulose-based printable resins in combination with gelatin methacryloyl (GelMA) and polyethylene glycol diacrylate (PEGDA) is not yet reported and holds promise in the biomedical engineering sector. Moreover, the outstanding fluorescent performance of amine-grafted TEMPO-CNCs/

GelMA/PEGDA hydrogels with tunable mechanical and biological properties for tracking cell migration, proliferation, and differentiation may serve as a novel approach in soft tissue engineering, especially for non-invasive monitoring of cells after surgery.

Herein, we fabricated a DLP printable bio-resin named GPCD resin. CNCs are the hydrolysis products of cellulose (Dutta, Hexiu, et al., 2021a; Dutta, Patel, et al., 2021b; Patel et al., 2022; Patil et al., 2022), and carboxylation of CNCs using TEMPO may promote higher dispersion stability, mechanical properties, improved electrochemical properties, and better cell adhesion (Gallagher et al., 2020; Ganguly et al., 2021; Ganguly et al., 2022). Amine-doped CDs (N-CDs) were synthesized using citric acid and urea *via* the hydrothermal method (Đorđević et al., 2022). The N-CDs were conjugated with T-CNCs *via* a one-pot amidation reaction through 1-ethyl-3(3-dimethyl aminopropyl) carbodiimide/N-hydroxysuccinimide (EDC/NHS) chemistry. The fabricated T-CNC@CDs exhibited strong excitation-dependent emission behavior in the visible spectrum. The proposed bio-resin is simple, easy to fabricate, eco-friendly, and highly biocompatible for cell encapsulation (Scheme 1). The as-prepared resin is mechanically robust, have desirable rheological properties, and exhibited excellent printability at ultra-low concentrations. Finally, simple and complex geometrical shapes were successfully printed to evaluate the printability of the formulated GPCD resin at room temperature. The 3D bioprinted GPCD hydrogels were tested to evaluate their biocompatibility toward full-thickness "skin" and "blood vessel" prototypes and showed the higher expression of cell differentiation markers. We envisage that the developed GPCD resin is non-toxic, exhibits ideal rheological properties for DLP printing, and successfully recapitulates the native microenvironment of the bio-inspired skin and vessel models. We believe that the developed bio-resin holds great promise for future soft tissue engineering, especially in image-guided tissue regeneration and clinical practice.

## 2. Experimental section

### 2.1. Materials, reagents, and instruments

2,2,6,6-(Tetramethylpiperidin-1-yl) oxyl (TEMPO) oxidized (carboxyl content: 0.3–2 mmol g$^{-1}$) cellulose nanocrystals (T-CNCs; 1 % solid content, width: 10–20 nm, length 50–400 nm) was obtained from the Cellulose Lab., Canada. Gelatin powder type B from porcine skin (purity: ≥99 %; gel strength: ~300 g bloom; 9000-70-8) and polyethylene glycol diacrylate (PEGDA; average M$_n$: 700; 26570-48-9), lithium phenyl-2,4,6-trimethylbenzoylphosphinate (LAP; 85073-19-4), N-hydroxysuccinimide (NHS; purity >98 %; 6066-82-6) were purchased from Sigma-Aldrich, USA. 1-(3-Dimethylaminopropyl)-3-ethyl-carbodiimide (EDC; purity >98 %, 25952-53-8) was obtained from TCI chemicals, Japan. A fully motorized Carima IM2 (Precision: 50 μm; curing depth: 0.1 mm, light uniformity: 99 %) DLP printer was obtained from Carima Corporation Ltd., Seoul, Republic of Korea. All the chemicals were used as obtained unless stated elsewhere.

### 2.2. 3D modeling and printer setup

The simple 3D models were designed using SolidWorks software (version 2022, Dassault Systems, France) and exported as STereo-Lithography (STL) file as demonstrated in our previous study (Dutta, Bin, et al., 2021c; Dutta, Hexiu, et al., 2021a). For organ-prototype printing, 3D anatomical models were exported from NIH 3D Print exchange program, released under Creative Commons CC-BY-SA license. The 3D CAD models were modified using open source Tinker CAD software provided by Autodesk, USA. Before fresh printing, all the STL files were sliced using custom-designed Slicer software (Carima Slicer, v2.0.3, Republic of Korea). The printable resin was directly used as a vat for the DLP printing. The DLP printer was equipped with a UV digital mirror device (DMD) of 365 nm UV-LED with average intensity of 400 lm, build resolution (*xy*) was 1920 × 1080 mm (engine resolution), and
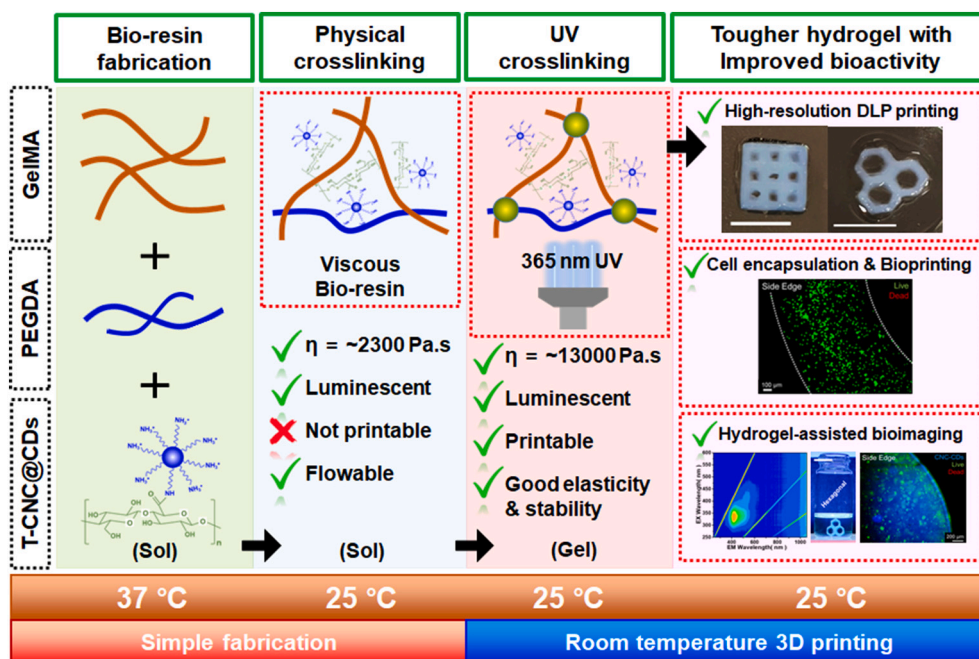
**Scheme 1.** Schematic illustration of the nanocellulose-based fluorescent bio-resin preparation and key features for image-assisted tissue regeneration study.

the build size (*xyz*) was 96 × 54 × 150 mm, respectively. The *z*-axis thickness and pixel size was set at 0.1 mm/layer and 50 μm. The overall dimension of the printer was 300 × 320 × 650 mm, respectively. The DLP printer was also equipped with an ultrafast curing module (CL1800, Carima, Republic of Korea) with 365 nm UV light source of 1800 W and an air cooling system.

### 2.3. Synthesis and characterization of N-CDs

The CDs was prepared from easily available and cost-effective precursor, citric acid (as carbon source) and urea (as nitrogen/amine source) *via* facile one-pot hydrothermal method. In a typical synthesis, citric acid (3 g) and urea (2 g) were dissolved in 25 mL DI water and stirred thoroughly. After that, the transparent solution was transferred into a Teflon-lined stainless steel autoclave (100 mL), and the hydrothermal process was conducted at 180 °C for 14 h. Next, the autoclave was cooled down in ambient temperature and the reaction product was dialyzed (MW cutoff: 100–500 Da) against DI water for 24 h. The dialyzed solution was centrifuged to remove agglomerated large particles and finally dried at 70 °C overnight to obtain a greenish-black powder, respectively. PL spectrometer (Quanta Master, Photon Technology, USA) and UV–Vis (Varian Cary 100, USA) spectrophotometer instruments were used to evaluate the optical properties of the CDs. High resolution transmission electron microscope (FE-SEM, JSM-7900F, Jeol, Japan) and atomic force microscope (AFM, Nanoscope5, Bruker, USA) was used to study the morphology and thickness of the CDs. Fourier transform Infra-Red (FT-IR, Frontier, Perkin Elmer, USA) spectrometer and X-ray photoelectron spectroscopy (XPS) were used to study the surface functional groups of the CDs. X-ray diffraction (XRD) spectra were collected using a Smart-Lab instrument (Rigaku, Japan) with a 4-kW X-ray generator and a D/teX Ultra 250 detector. Raman spectra were recorded *via* micro-Raman spectroscopy (ANDOR Monora500i, 633 nm, Oxford Instruments, UK).

### 2.4. Synthesis of N-CDs modified cellulose nanocrystals (T-CNC@CDs)

The grafting of CDs onto T-CNCs was performed as reported elsewhere with slight modification (Quraishi et al., 2019). In a typical synthesis, 200 mL of T-CNCs (1 wt%) was stirred for 30 min, followed by addition of EDC (0.83 g) and NHS (3.2 g) for 2 h to charge the carboxylic groups of the T-CNCs. After stirring, 10 mL of aqueous N-CDs solution (2 mg/ mL) was injected into the reaction mixture and allowed to stir overnight at ambient temperature. The resulting solution was dialyzed (MW cutoff: 12–14 kDa) against DI water for 24 h to remove the unreacted salts and CDs. The final product was stored at 4 °C until further use.

### 2.5. Characterization of the T-CNC@CDs

To confirm the grafting of N-CDs on to the surface of T-CNCs we performed the TBO staining. The reduction/addition of carboxylic groups (-COO) in pure T-CNCs can be quantified using this technique (Cometta et al., 2022). Briefly, the pure T-CNC and T-CNC@CDs (1 wt%, 5 mL) were taken in a glass vial and incubated with 0.5 mM TBO (pH 10.0, Sigma-Aldrich, USA). The mixture was stirred for 5 h at room temperature. After that, the mixture was centrifuged at 10,000 rpm to pellet down the T-CNC and T-CNC@CDs. The pellet was washed thrice with 0.1 mM NaOH (pH 10.0) until excess TBO is washed off. Next, the pellet was resuspended in 50 % (v/v) acetic acid and kept stirring for 10 min. After that, the mixture was again centrifuged and the supernatant was taken into a 96-well plate. The absorbance was recorded at 633 nm using a spectrophotometer. Additionally, a standard curve of known amount of TBO (0–1 mM) was prepared in 50 % acetic acid. The reduction of carboxylic group (mmol $g^{-1}$) was calculated assuming an equal binding ratio (1:1) of TBO and carboxylic groups.

The zeta potential of the unmodified T-CNCs and T-CNC@CDs was measured using a particle size analyzer (Zetasizer v7.13, Malvern Panalytical, UK). The sample concentration was taken at 0.8 % and at least three independent experiments were performed.

The surface functional group and chemical moieties of the T-CNCs and T-CNC@CDs was evaluated using XPS (Kα+, Thermo-Fischer, USA) survey spectra and high-resolution XPS spectra at C1s, N1s, and O1s, respectively. The XPS spectra was recorded with AlKα source with an operating energy of 150 eV.

The structural property of the T-CNCs and T-CNC@CDs was measured using an XRD (X'Pert Pro MPD, Philips, Netherlands) using an operating voltage and current of 40 kV and 40 mA, with a CuKα monochromatic gun (λ = 1.5414 A°). The derived spectra were used for

the calculation of crystallinity index (CI) using Segal method (Patel et al., 2023) (Eq. (1)):

$$Crystallinity\ Index\ (CI) = \frac{I_{200} - I_{am}}{I_{200}} \times 100\% \qquad (1)$$

Where, $I_{200}$ represents the peak intensity at (200) diffraction plane, and $I_{am}$ indicates the maximum intensity between the (200) and (114) diffraction plane, respectively.

### 2.6. Synthesis of gelatin methacryloyl (GelMA)

The GelMA was synthesized as reported earlier (Geng et al., 2021; Liu et al., 2019; Nichol et al., 2010). Briefly, gelatin (10 % *w/v*) was dissolved in DW (100 mL) at 50 °C under vigorous stirring. After that, the solution temperature was adjusted to 40 °C and methacrylic anhydride (2 mL) was injected into the gelatin solution, and reacted for 2 h. Next, the reaction was stopped by adding warm PBS (5-fold) and dialyzed (MW cutoff: 12–14 kDa) against DW for 3–5 days to remove the acrylic acid, respectively. Finally, the dialyzed product was concentrated, frozen in −80 °C for 12 h, and finally lyophilized using vacuum dryer for 4–5 days to obtain a white foam. The as-obtained white foam was stored at 4 °C until further use. The as-synthesized GelMA (30 mg in D$_2$O) was characterized by the $^1$H NMR using a Bruker NMR (600 MHz, Bruker Avance Neo-600, Bruker, USA). For the degree of substitution (DS) analysis, the NMR spectra was normalized to the phenylalanine signal ($\delta = 7.2$–$7.4$ ppm) of gelatin and then integrated into the vinyl proton ($\delta = 5.4$–$5.6$) of both gelatin and GelMA. The DS was calculated using following Eq. (2):

$$DS = \left(1 - \frac{A_H\,(5.4\&5.6)\ of\ GelMA}{A_H\,(5.4\&5.6)\ of\ Gelatin}\right) \times 100\% \qquad (2)$$

### 2.7. Fluorescent resin preparation and DLP printing

The photocurable resin was prepared by mixing the prepolymer, photoinitiator, and T-CNCs@CDs, respectively. Briefly, T-CNCs@CDs (0.8 wt%) was stirred for 30 min at 40 °C, followed by addition of GelMA (0.5 wt%) and PEGDA (0.1 wt%) until fully dissolved and form a transparent solution. After that, 0.25 % (*w/v*) LAP photoinitiator was added the resin solution and allowed to stir for 30 min at dark condition. The as-prepared resin (GPCD) was used as a vat for 3D printing and was stored at 4 °C for reuse. To prevent the over-curing of the resin beyond the focal plane, the *z*-axis print-bed was washed properly with 70 % (*w/v*) ethanol to remove any debris form the surface.

For 3D printing, the simple square (infill density: 15 % and 30 %; number of layers: 20 and 40) and hexagonal (number of hexagons: 3, 4, and 6; number of layers: 20 and 40) models were designed using SolidWorks software and exported as STL file, followed by slicing with Carima Slicer. The *z*-axis thickness was set at 0.1 mm/layer to produce high-quality 3D structures. The layer-by-layer printing was carried out by regulating the *z*-axis platform. The printing parameters were used as follows: 50 μm resolution, 4 s of initial exposure, 11.8 s of basic exposure, and 5 s of curing time for buffer layers. After 3D printing, each constructs were carefully removed from the platform, rinsed with DW, and finally cured with CL1800 Carima (Carima, Republic of Korea) module. For organ prototype printing, ear, blood vessel, muscle, and skin models were printed carefully to test the printing quality of the resin. After printing, all the prototype models were rinsed with DW and subsequently cured to remove the unreacted polymers. Likewise, the GelMA (GM), and GelMA-PEG (GPD) resins were also tested as a control samples. The printing accuracy of the printed hydrogels were determined using following (Eq. (3)):

$$Printing\ accuracy = \frac{No.\,of\ correct\ predictions}{Total\ no.\,of\ predictions} \times 100 \qquad (3)$$

### 2.8. Characterization of the 3D printed hydrogels

#### 2.8.1. Morphology and interaction study

The morphology of the printed hydrogel scaffold and thin films was analyzed by FE-SEM (JSM-7900F, Jeol, Japan) with an accelerating voltage of 10 kV cm$^{-1}$. FT-IR spectrometer (Frontier, Perkin Elmer, UK) and XRD (X'Pert Pro MPD, Philips, UK; $2\theta = 10°$-$60°$ range) were used to study the interaction and structural changes of the pure and T-CNC@CDs incorporated hydrogels. The bulk hydrogel scaffold was used for FT-IR analysis. The kinetics of photopolymerization was studied using ATR-FTIR (iN10/iS50, Thermo Scientific, USA) spectroscopy with a DLaTGS detector system (450–7600 cm$^{-1}$). For this, the resin solution was taken between two glass slides separated by a 0.4 mm silicone spacer and exposed to the UV light for various time points. After that, the hydrogel film was directly analyzed using ATR-FTIR mode. The degree of double bond conversion (DC) was calculated using following Eq. (4):

$$DC\ (\%) = \left(1 - \frac{Peak\ intensity\ of\ vC - C}{Peak\ intensity\ of\ vC = C}\right) \times 100 \qquad (4)$$

The compressive strength of the 3D printed hydrogels were tested using a universal tensile machine (UTM, A&D Digital, Japan), respectively.

#### 2.8.2. Swelling and degradation study

The *in vitro* swelling properties of the freeze-dried 3D printed scaffolds (GM, GPD, and GPCD; $1 \times 1 \times 0.5$ mm dimension) were evaluated as reported in our pervious study (Dutta, Hexiu, et al., 2021a). Briefly, known amount of weights (~10 mg) of the freeze-dried scaffolds were immersed in water for 24 h and kept at 37 °C. After 24 h, the scaffold surface was gently blotted to remove the excess water. The swelling efficiency was determined using following Eq. (5):

$$\%swelling\ efficiency = \frac{W_s - W_d}{W_s} \times 100 \qquad (5)$$

Where, $W_d$ and $W_s$ indicates the weight of the scaffolds before and after swelling. The degradation kinetics of the developed scaffolds were evaluated by immersing the scaffolds ($1 \times 1 \times 0.5$ mm) in PBS and trypsin (1 mg/mL; Sigma-Aldrich, USA; 9002-07-7) solution as reported in our previous literature (Patel et al., 2022). Briefly, 10 mg of hydrogel scaffolds were immersed into PBS or trypsin solution (5 mL of each) at 37 °C. After desired time points, the scaffolds were taken out, dried, and the weights were measured. The degradation behavior of the scaffold was calculated using following Eq. (6):

$$Weight\ loss\ (wt.\%) = \frac{W_i - W_d}{W_i} \times 100 \qquad (6)$$

Where, $W_i$ and $W_d$ indicates the weight of the scaffolds before and after degradation.

#### 2.8.3. Surface wettability measurements

The surface wettability of the fabricated hydrogel scaffolds was assessed using a contact angle device (SEO Phoenix-MT, Republic of Korea) equipped with a high-resolution CCD camera.

#### 2.8.4. Rheological measurements

The viscoelastic nature of the developed hydrogels was evaluated using a rotational rheometer (ARES-G2, TA Instruments, New Castle, USA) with a parallel plate of 10 mm and measuring gap value of 0.25 mm. The frequency sweep ($\omega$) test was conducted in the range of 0.1 to 100 Rad s$^{-1}$ with 1 % strain rate at 37 ± 2 °C. Amplitude sweep tests were conducted to measure the storage (G′) and loss modulus (G″) of the hydrogels. The recovery strength of the GM, GPD, and GPCD hydrogels was evaluated with varying shear rates (0.1, 100, and 0.1 s$^{-1}$) for different time points (0–100, 101–200, and 201–300 s), at 37 ± 2 °C. The photo-rheology measurements were also conducted to determine

the effect of UV crosslinking on the hydrogel's viscoelasticity before and after addition of T-CNC@CDs.

### 2.8.5. DSC measurements

The DSC thermal analysis was carried out using DCS 2500 (TA Instruments, New Castle, USA). For DSC measurements, the 3D printed hydrogel scaffolds were dried at ambient temperature until reaching a constant weight. After that the samples were subjected to thermal analysis of a dynamic cycle from 25 °C to 150 °C at a heating rate of 10 °C min$^{-1}$. TA Trios v3.3 (TA Instruments, USA) software was used to analyze the data.

### 2.8.6. Small angle X-ray scattering (SAXS) analysis

One of major challenges of vat polymerization is the aggregation of nanomaterials during 3D printing. Therefore, the homogenous distribution of nanomaterials inside polymer matrix is crucial for high-resolution 3D printing. To evaluate the scattering pattern of the T-CNCs, T-CNC@CDs, and T-CNC@CDs/GelMA-PEGDA complex, the SAXS patterns were obtained using Xeuss 2.0 (Xenocs SAXS, France) device. The device was equipped with a CuK$_\alpha$ monochromatic gun and a three-point collimation (sample to detector distance: 2500 mm), and a 300 K detector system (3 modules, pixel size: $172 \times 172$ μm$^2$, silicon diode array). The scattering intensity I($q$) was recorded and the scattering vector is defined as $q = 4\pi/\lambda \sin\theta$, where $2\theta$ and $\lambda$ indicates the scattering angle and wavelength, respectively. All the measurements were performed under vacuum condition at ambient temperature. The eccentricity ($E$) value was calculated from the 2D SAXS pattern by assuming the pattern as ellipse using the following Eq. (7):

$$E = \sqrt{1 - \frac{b^2}{a^2}} \tag{7}$$

### 2.8.7. Surface topography and roughness analysis

The surface roughness and topography of the developed hydrogels was evaluated using atomic force microscopy (Nanoscope 5, Bruker, USA). For this, GM, GPD, and GPCD hydrogels ($2.5 \times 0.5$ mm) were carefully printed using the DLP printer and post-cured using a 365 nm U$V$ chamber for 15 min. After that, the round-shaped hydrogel discs were allowed to dry at ambient temperature for 2–3 days in a sterile environment. The dried films were directly visualized by the AFM using tapping mode in the air with silicon V-shaped cantilevers.

### 2.8.8. Measurement of fluorescence (FL) stability

The FL stability of the DLP-printed GPCD hydrogel was assessed by both qualitative and quantitative assays. For qualitative study, the freshly printed GPCD hydrogel ($5 \times 5$ mm) was immersed in various pH buffers (6.5, 7.4, and 9.5) up to 30 days. After desired time points, the hydrogels were taken out from the buffer solution, blotted, and photographed using an inverted FL microscope (DMi8, Leica, Germany) with an excitation of 405 nm, respectively. Pure GelMA hydrogel was taken as control set. The FL signal from GPCD hydrogel was normalized to the pure GelMA hydrogel to calculate the original FL emission of the GPCD hydrogel. For quantitative analysis, the FL signal intensity was measured using a PL spectrophotometer (PTI Quanta Master-300, Photon Technology, New Jersey, USA) and the data was represented as mean signal reduction (%) with respect to the time.

### 2.9. In vitro experiments

### 2.9.1. Cell line and maintenance

Human dermal fibroblast (hDFs, PCS-201-012), primary epidermal keratinocytes (hKCs, PCS-200-011), and mouse myofibroblasts (C2C12, CLR-1772) were obtained from American Type Culture Collection (ATCC), USA. The hDFs, KCs, and C2C12 were maintained in DMEM/ Ham's F12 media (Welgene, Republic of Korea, 1:1 ratio; LM002–01) supplemented with 10 % FBS (Sigma-Aldrich, USA; F2442), and 1 %

antibiotics (P/S, Thermo Scientific, USA; 15240096). For endothelial differentiation, the hDFs were additionally grown on endothelial basal media (EBM, Gibco-BRL, USA; C-22010).

### 2.9.2. In vitro cytotoxicity evaluation

The cytotoxicity profile of the fabricated hydrogels (GM, GPD, and GPCD) was assessed using WST-8 assay. For this, hDFs ($1.5 \times 10^4$ cells/ 100 μL/96-well) were seeded with hydrogel samples (50 mg each) and incubated for 7 days. After specific time interval, the cells were washed with PBS and incubated with 10 μL of WST-8 (DoGen Bio, Republic of Korea) dye and the viability was measured spectrophotometrically (Infinite M Nano, TECAN, Switzerland). To test the biocompatibility of the 3D printed structures, a prototype model of tubular construct, muscle, skin, and ear were printed using GPCD bio-resin and sterilized using UV irradiation. After that, the printed hydrogels were incubated with DMEM media for 24 h to remove the unreacted polymers or crosslinkers. Approximately $4 \times 10^4$ cells/2 mL (hDF, hKCs, and C2C12) were cultured with the printed constructs in a 6 well plate and incubated for 5 days. The old media was replaced every another day. Afterwards, the cytotoxicity was evaluated using a Live/Dead Staining Kit (Sigma-Aldrich, USA) according to the manufacturer's instruction. Briefly, the cells were carefully washed with $1\times$ PBS and supplemented with fresh DMEM media containing 10 μL of Live/Dead dye. Next, the cells were incubated at 37 °C for 5–10 min. After desired staining, the cells were washed with PBS and visualized by an inverted fluorescence microscope (DMi8, Leica, Germany) with 488 nm and 514 nm excitation channels. The images were captured with $10\times$ objective lens. The percentage of viable cells were calculated from three independent images using ImageJ (v1.8, NIH, Bethesda, USA) software.

### 2.9.3. 3D bioprinting and cell movement tracking

Based on the initial cytotoxicity evaluation, we have selected the GPCD bio-resin for 3D bioprinting analysis. For bioprinting, the resin precursors (GelMA, PEGDA, T-CNC@CDs, and photoinitiator) were sterilized using UV treatment and dissolved in sterile DMEM media (serum free). After that, the resin solution (15 mL) was mixed with the hDFs to achieve a final cell density of $2.5 \times 10^4$, respectively. Next, the hDF-laden resin was gently pipetted and incubated at 37 °C for 5 min. After desired incubation, the bio-resin was transferred into the resin vat and bioprinted using a pre-designed structure ($5 \times 5$ mm). The printing resolution was set at 0.1 mm/layer and a total of 25 layers were printed. After DLP printing, the constructs were carefully detached from the platform and incubated with fresh DMEM media containing serum and antibiotics. For epidermal differentiation, the hDF-laden constructs were incubated with DMEM/Ham's F12 supplement for 3 days. For endothelial growth, the hDF-laden constructs were supplemented with EGM, respectively.

The cytotoxicity profile of the bioprinted hDFs were assessed using Live/Dead assay after 3 days of incubation. For the tracking of hDFs inside the fluorescent hydrogel, we have photographed the hDFs using 488 nm (Live), 514 nm (Dead), and 405 nm (for hydrogel) excitation filters. To visualize the cellular infiltration in $z$-direction, we further observed the cells using cross-section of the hydrogel. To confirm the cell infiltration inside the GPCD hydrogel, we conducted a time-dependent imaging of hDFs and hKCs up to 30 days (one month). The images were processed and analyzed with ImageJ software.

Next, the F-actin morphology of the hKCs was assessed through immunofluorescence staining after 21 days of culture to understand the actin distribution and infiltration inside the GPCD hydrogel. For this, the hKCs (initial cell density: $4 \times 10^4$/bioink)-laden hydrogels were harvested after 7, 14, and 21 days of culture and fixed with 3.7 % paraformaldehyde (Sigma-Aldrich, USA) for 20 min. After fixation, the constructs were permeabilized with 0.1 % Triton-X 100 for 10 min and blocked with 1 % normal goat serum (Gibco-BRL, USA) for 1–2 h. After blocking the printed constructs were rinsed with PBS for 10 min, and incubated with Rhodamine-conjugated F-actin probe (AAT Bioquest,

USA) for 90 min at room temperature. After that, the constructs were carefully sectioned into thin slice and dipped into the DAPI solution (Sigma-Aldrich, USA) for 30 s. Next, the hydrogel slices were rinsed in PBS and photographed using an inverted fluorescence microscope (DMi8, Leica, Germany) with $40\times$ objective lens. The cell perimeter and F-actin intensity was measured using ImageJ software (v1.8, NIH, Bethesda, USA) with Fiji plugins. At least five individual images were assessed for quantification analysis.

### 2.9.4. Immunocytochemical (ICC) analysis

To evaluate the expression of CD31 marker, we performed immunocytochemistry of the bioprinted construct after 3 days of incubation. For this, the bioprinted hDFs were induced with EGM for 3 days. Next, the bioprinted cells were fixed with 3.7 % paraformaldehyde (Sigma-Aldrich, USA; 50-00-0) for 15 min at room temperature. After fixation, the construct was permeabilized with 0.1 % Triton-X 100 (Sigma-Aldrich, USA; 9036-19-5) for 10–20 min at room temperature. Next, the fixed and permeabilized construct (bulk or cross-section) was blocked with 1 % bovine serum albumin (Sigma-Aldrich, USA) for 3 h. After blocking the construct was washed with PBS and incubated with primary antibody against CD31 (Santa Cruz Biotechnology, USA, sc-376764, dilution; 1:500) and cytoskeletal protein vinculin (Santa Cruz Biotechnology, USA, sc-73614, dilution; 1:500), followed by incubation with fluorescent secondary antibodies (Santa Cruz Biotechnology, USA; sc-516140, dilution; 1:250). After desired staining, the bioprinted construct was incubated with 100 μL of DAPI (Sigma-Aldrich, USA; 28718-90-3) to stain the nucleus. Next, the bioprinted construct was washed and carefully placed over a microscopic slide equipped with grooved surface and a few drops of PBS was added to avoid dehydration of the sample. The images were collected using an inverted fluorescence microscope (DMi8, Leica, Germany) with proper excitation filers and processed with ImageJ software.

### 2.10. Quantitative real-time PCR (qRT-PCR) analysis

The cell differentiation capability of the hDF, C2C12, and hKCs in various biomimetic models (vessel, muscle, skin, and ear) were evaluated by profiling their gene expression using qRT-PCR analysis after 5 days of culture. The detailed method of qRT-PCR study is reported in our previous literature (Dutta, Hexiu, et al., 2021a). The qRT-PCR experiment was conducted in triplicate ($n = 3$) and GAPDH gene marker was used as housekeeping gene for the experiments. The specified gene primers used for qRT-PCR analysis is listed in Table S2. All the primers were obtained from BIONEER Inc., Daejeon, Republic of Korea.

### 2.11. Image analysis

The image analysis was carried out using ImageJ software (v1.8, NIH, Bethesda, USA) with Fiji plugins. The pore diameter and pore depth of the scaffolds was calculated using the ImageJ software with *size analyzer* tool. At least 3 independent images were assessed in each group to calculate the pore diameter. The quantification of Live/Dead (%) assay was performed using the Fiji plugins with *Live Cell Counter* tool as per JavaScript command. The FL images of the 3D bioprinted hydrogels with different channels (Live/Dead assay, CD31, and vinculin expression) were merged using ImageJ software (image > color > merge) in RGB format. The cell perimeter and F-actin intensity was calculated using 8-bit images. The FL images were first converted to 8-bit from RGB color and the color threshold was adjusted. After that the F-actin intensity was calculated by subtracting the total actin intensity/actin intensity over DAPI and represented as bar histogram.

### 2.12. Statistical analysis

The statistical analysis was carried out using One-way analysis of variance (ANOVA) test by Origin Pro v9.0 software (Origin Lab,

Massachusetts, USA). Data were presented as mean $\pm$ s.d. of triplicate ($n = 3$) experiments, statistical significance was considered at $*p < 0.05$.

## 3. Results and discussion

### 3.1. Characterization of T-CNCs and N-CDs

The T-CNCs were directly utilized for the synthesis of T-CNC@CD complexes. Fig. 1a(i) shows the high-resolution transmission electron microscopy (HR-TEM) image of the T-CNCs. The average length and width of the T-CNCs were calculated to be $284 \pm 24$ nm and $21 \pm 0.8$ nm, respectively. The average height of the T-CNCs was 3–6 nm, as evaluated using the atomic force microscopy (AFM) image (Fig. 1a(ii)). The blue-emissive N-CDs were synthesized *via* condensation polymerization of citric acid and urea through a hydrothermal method, where citric acid and urea served as the carbon and amine source, respectively. The polymerization resulted in polymer-like dots, which were further carbonized at 180 °C to form N-CDs (Zhang, He, et al., 2015a). The structural properties of the N-CDs were evaluated by HR-TEM and AFM analysis. As shown in Fig. 1a(iii), the N-CDs exhibited a unique spherical morphology of amorphous carbon particles with diameters ranging from 3 to 5 nm. The average height of the N-CDs was 1.5 nm, as shown in Fig. 1a(iv). The XRD pattern (Fig. S1a) of the N-CDs showed a broad diffraction peak at 25.67°, representing a highly disordered carbon structure (Niu et al., 2013). Moreover, the Raman spectra of the N-CDs exhibited a broad peak at approximately 1250 cm$^{-1}$ owing to the presence of C—C (Sp$^3$ carbon framework) and C—O vibrations. The peak at approximately 1590 cm$^{-1}$ corresponds to the G-band, representing the Sp$^2$ carbon framework. The mixed peak around 1225–1260 cm$^{-1}$ corresponds to the D-band, indicating the presence of defects or disordered carbon frameworks due to thermal condensation (Fig. S1b).

Furthermore, the chemical composition, surface functional groups, and the optical property of the as-prepared N-CDs were investigated using XPS and UV–Vis spectroscopy. The XPS spectroscopy was performed to evaluate the presence of C1s, O1s, and N1s in the region of 285.2, 400.8, and 536.4 eV, indicating the doping of nitrogen/amine moieties (Fig. S1(c)). The high-resolution XPS spectra at C1s showed the presence of three peaks at 285.5, 287.6, and 289.4 eV corresponding to the C-C/C=C, C—N, and C-O/C=O, respectively, of the carbon framework (Fig. S1d). The XPS spectra of N-CDs at N1s exhibited two peaks at 400.0 and 401.9 eV, corresponding to the –C-N and graphitic N/N-H groups (Fig. S1e). Therefore, based on the surface chemistry and functional group analysis, it was evident that the as-prepared N-CDs were mainly composed of -OH, N—H, C=C/C=N, and C-C/C-N bonds (Meierhofer et al., 2020). The UV–Vis spectra of the N-CDs showed a peak around 329 nm (Fig. S1(f)) with unique blue fluorescence property. Taken together, our results demonstrate that the as-prepared N-CDs are highly amorphous with spherical/oval geometry and contains amine moieties on the surface.

### 3.2. Characterization of T-CNC@CDs

N-CDs were incorporated onto the T-CNCs *via* chemical grafting. The N-CDs were used as the model CD not only because of their simple fabrication technique but also because of their excellent biocompatibility and aqueous solubility (Bhatt et al., 2020; Quraishi et al., 2019). Moreover, hydrothermally prepared CDs exhibited a higher quantum yield and showed a minimum loss of fluorescence during surface modification with other nanomaterials (Đorđević et al., 2022; Quraishi et al., 2019). Chemical grafting was accomplished by the conventional EDC/NHS-mediated amidation reaction to form T-CNCs@CDs complexes. The physical immobilization of CDs is comparatively simple and relies on electrostatic interactions between the carboxyl and ammonium ions; however, the yield is very low. Fig. 1(b) schematically represents the grafting of the N-CDs onto the surface of the T-CNCs. The surface functionalization was confirmed using TBO staining, zeta potential, and
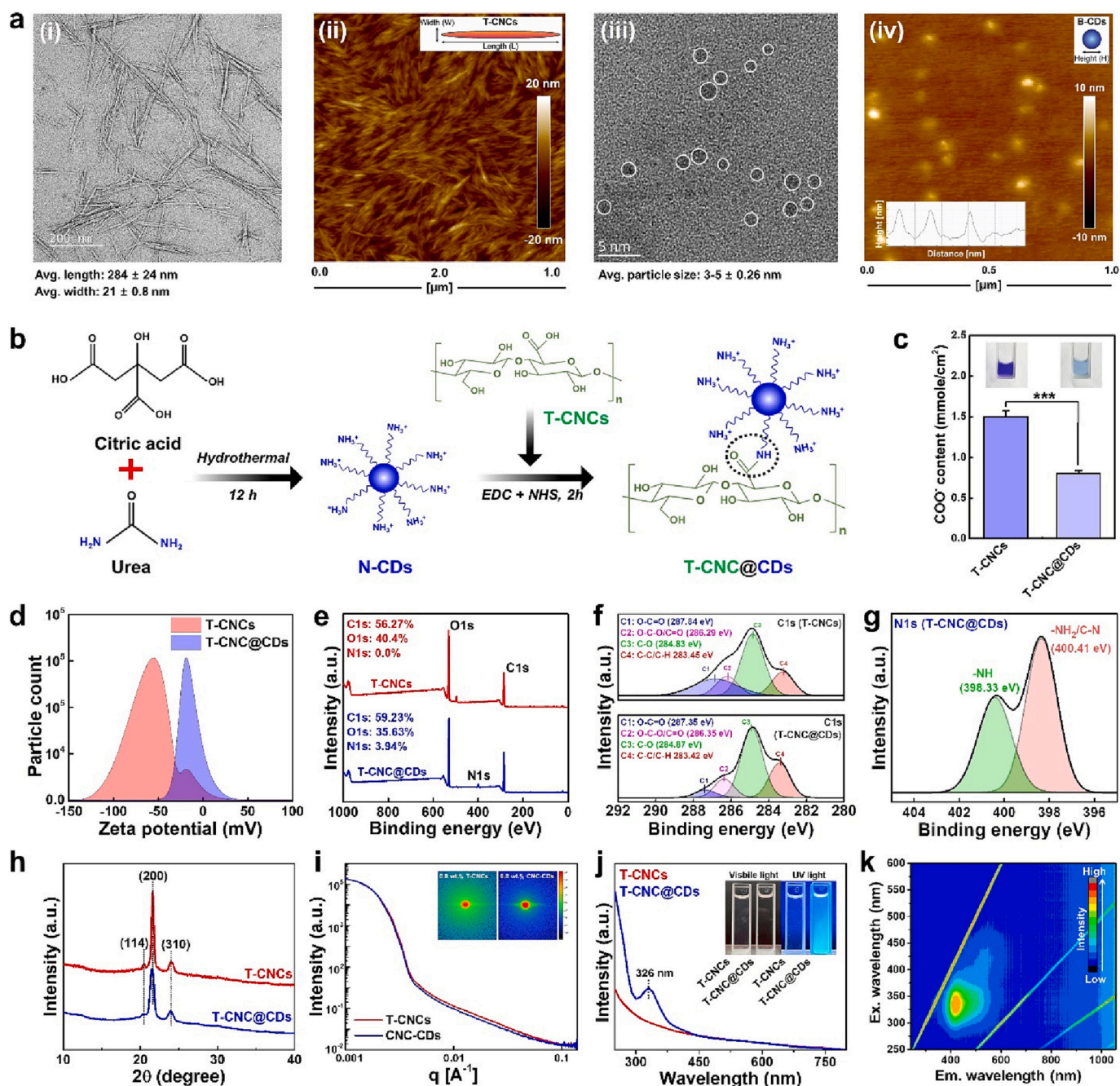
**Fig. 1.** Preparation and characterization of the T-CNC@CDs nanocomposites. **(a)** HR-TEM and AFM phase images of the T-CNCs and N-CDs showing the unique road-shaped and spherical morphology. Scale bar: (i) 200 nm, (ii) 2 μm, (iii) 5 nm, and (iv) 0.5 μm. **(b)** Schematic illustration of the N-CDs synthesis and functionalization of T-CNCs *via* amide coupling. **(c)** Estimation of carboxylic group density of T-CNCs and T-CNC@CDs before and after amide coupling using TBO staining (***$p <$ 0.001). **(d)** Zeta potential of the T-CNCs and T-CNC@CDs. **(e)** XPS total survey spectra of T-CNCs and T-CNC@CDs. High-resolution C1s **(f)** and N1s **(g)** spectra of the nanocomposites. **(h)** XRD spectra of the T-CNCs and T-CNC@CDs. **(i)** SAXS patterns of the T-CNCs and T-CNC@CDs showing the dispersion stability in water. **(j)** UV–Vis spectra of the T-CNCs and CNC-CDs. Insets are water dispersed T-CNCs and CNC@CDs under visible and UV light. **(k)** PL emission spectra of the T-CNC@CDs.

XPS spectroscopy analysis. The TBO staining was conducted to determine the reduction of carboxylic (-COO⁻) charge density on the surface of T-CNCs, before and after modification. As shown in Fig. 1(c), the N-CDs grafting significantly reduced the COO- density (indicated by the reduction of blue color) of the T-CNCs, suggesting the surface modification. To confirm this, we next evaluated the zeta potential (ζ) of the T-CNCs and T-CNC@CDs, and the result is depicted in Fig. 1(d). The surface charge density of the T-CNCs and T-CNC@CDs were calculated to be $-52.06 \pm 1.4$ and $-28.3 \pm 0.65$, respectively. A decrease in ζ-value was probably due to the grafting of N-CDs (Zhang, Zhang, et al., 2015b).

The chemical modification and surface functional groups of the T-CNCs and T-CNC@CDs was analyzed using XPS survey and the results are shown in Fig. 1(e). The T-CNCs exhibited two typical peaks at 292.48 (56.27 %) and 534.91 eV (40.4 %) corresponding to the C1s and O1s spectra. Whereas, the T-CNC@CDs showed three peaks around 293.58 (59.23 %), 406.28 (3.94 %), and 533.78 eV (35.63 %) owing to the presence of C1s, N1s, and O1s spectra, indicating the presence of doped N-CDs. The high-resolution C1s spectra of both T-CNCs and T-CNC@CDs displayed characteristic peaks for O-C=O (287.84 eV), O-C-O/C=O (286.29 eV), C—O (284.83 eV), and C-C/C-H (283.45 eV) bonds (Fig. 1

(f)), indicating the predominant structure of nanocellulose (Patel et al., 2023). Furthermore, the high-resolution N1s spectra of T-CNC@CDs showed two predominant peaks at around 398.33 (44.23 %) and 400.41 eV (59.78 %) owing to the presence of –NH (amide) and –NH$_2$/C-N (protonated nitrogen/carbon bound to nitrogen) bonds (Fig. 1(g)), which was not observed in T-CNCs (Fig. S2). Thus, in agreement with previous study (Zhao et al., 2017), our results confirm that the T-CNCs was successfully aminated *via* coupling with N-CDs.

The structural property and dispersion stability of T-CNC@CDs were evaluated using XRD and small angle X-ray scattering (SAXS) analysis. The XRD spectra (Fig. 1(h)) of the pure T-CNCs exhibited characteristic peaks at 20.42°, 21.59°, and 23.94°, respectively corresponding to the

114, 200, and 310 planes of the typical cellulose-I structure (Cheng et al., 2017; Dutta, Patel, et al., 2021b). The crystallinity index of T-CNCs was found to be 70.24 %. Notably, N-CD incorporation slightly decreased the crystallinity (~64.3 %) of T-CNCs, indicating successful grafting of N-CDs owing to their amorphous nature. The crystallite size of T-CNCs (2θ = 21.59°) and T-CNC@CDs (2θ = 21.42°) was calculated to be 2.8 nm and 2.4 nm, respectively.

Because CNCs are known to display concentration-dependent self-assembly behavior in an aqueous state (Habibi et al., 2010; Tran et al., 2020), we examined the dispersion stability of T-CNCs (0.8 wt%) and T-CNC@CDs (0.8 wt%) in aqueous condition using SAXS analysis (Fig. 1 (i)). However, low concentrations of CNCs exhibited weak self-assembly
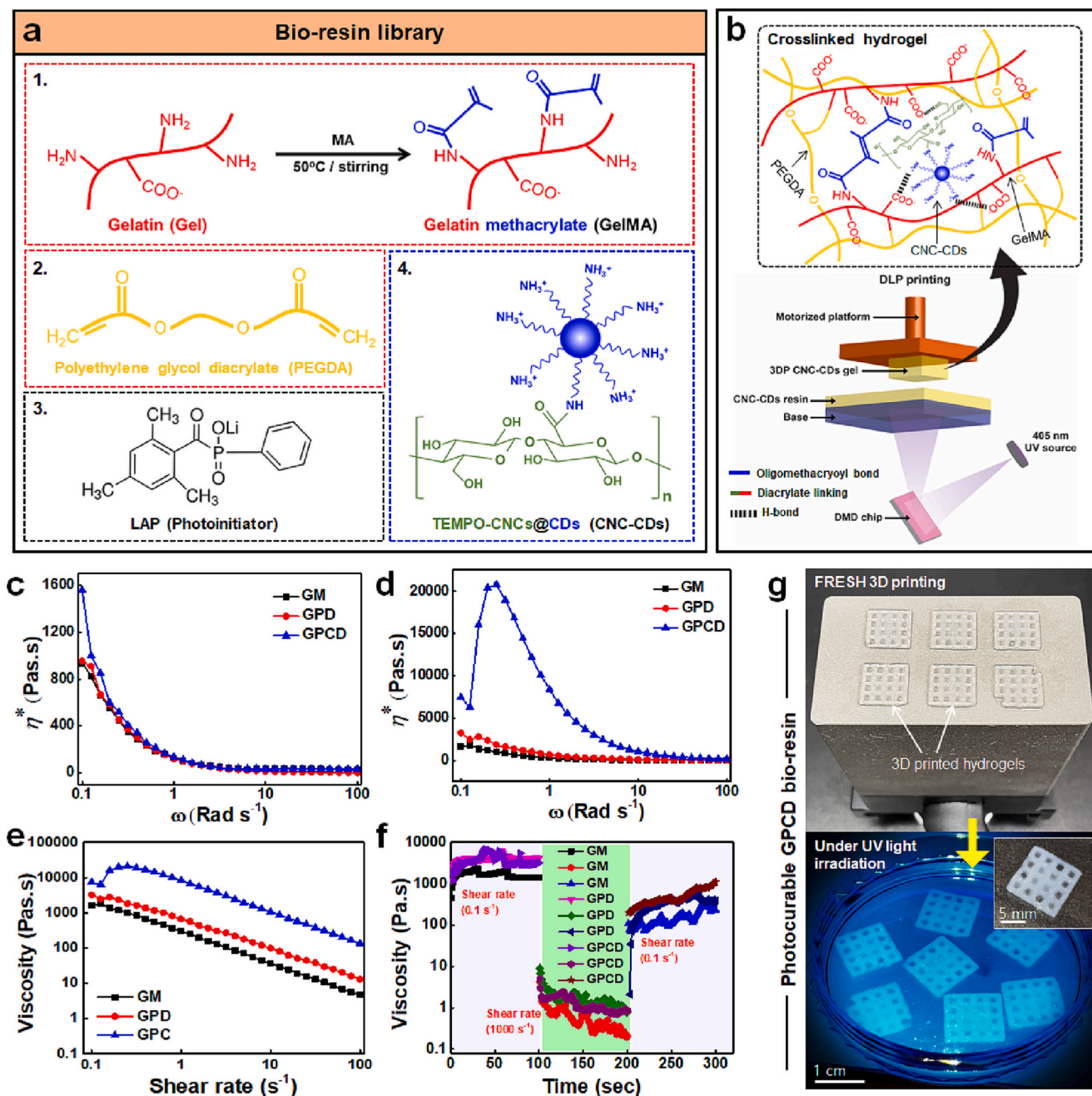


**Fig. 2.** Fabrication and characterization of the T-CNC@CDs based fluorescent bio-resin for DLP printing. **(a)** Schematic illustration of the polymer library used for bio-resin preparation. **(b)** Schematic illustration for the DLP printing and crosslinking process. Frequency sweep (ω) test of the GM, GPD, and GPCD bio-resins at 25 °C within 0.1 to 100 Rad s$^{-1}$ range, **(c)** before and **(d)** after photocrosslinking. The complex viscosity of the bio-resin is denoted as $\eta^*$. **(e)** Viscosity ($\eta^*$) *vs.* shear rate (s$^{-1}$) curve of the developed bio-resins showing the shear-thinning nature. **(f)** Thixotropic behavior of the GM, GPD, and GPCD bio-resins. **(g)** Digital photograph of the 3D printing process and the printed GPCD hydrogels. Scale bar: 5 mm and 1 cm.

properties owing to the higher dispersion stability and availability of local nematic islands near the 1/N* transition state. The dispersion stability of nanomaterials is crucial for 3D printing applications (Dutta, Hexiu, et al., 2021a; Tran et al., 2020). In agreement with previous studies, (Cohen et al., 2019) our results demonstrated that 0.8 wt% T-CNCs exhibited weak assembly behavior, which was characterized by a low $q_0$ value ($d = 137$ nm) within 0.001 to 0.01 A$^{-1}$ range. A similar pattern was observed for the T-CNC@CDs composites ($d = 138$ nm), suggesting that the inter-particle distance was higher in the solution state. The 2D SAXS patterns of T-CNCs and T-CNC@CDs exhibited similar trends, indicating that both components are highly dispersed in the aqueous state. The T-CNCs@CDs exhibited bright fluorescence under 365 nm UV light irradiation, whereas T-CNCs showed no noticeable fluorescence, suggesting that the N-CDs fluorescence property was not decreased after modification (Fig. 1(j)). Owing to the higher aqueous dispersibility, the T-CNC@CDs exhibited an excitation-dependent emission behavior (350–800 nm) when excited with various wavelengths, with a photoluminescence (PL) emission maximum ($\lambda_{em}$) at 530 nm corresponding to the greenish-blue emission (Fig. 1(k)). Taken together, our results demonstrated that the N-CDs was successfully grafted onto the surface of T-CNCs and the inherent structural property was retained after modification, which could be useful for fabrication of fluorescent hydrogels.

### 3.3. Structural, functional, and mechanical properties of the fluorescent bio-resin

The synergistic integration of nanofillers with DLP printing can enable the development of various biomimetic architectures with unprecedented level of biological properties. In this context, fabrication of resins with attractive fluorescent properties may have various application in regenerative medicine, especially in non-invasive therapeutics (Elder et al., 2020). Fig. 2(a) shows a schematic overview of the resin library used for the fabrication of fluorescent bio-resins. Photocurable biopolymers, such as gelatin methacrylate (GelMA) and polyethylene glycol diacrylate (PEGDA), were used as the polymer source, LAP was used as the photoinitiator, and T-CNC@CDs were used as nanofillers in this study. The composition of the bio-resin is presented in Table S1. The as-synthesized GelMA was freeze-dried to obtain a foam-like structure with a degree of substitution (DS) of approximately 70 %. The $^1$H NMR spectra of GelMA showed characteristic resonance signals at $\delta = 5.4$ and 5.6 ppm (Fig. S3a), corresponding to the vinyl protons [2H$^+$] of the methacryloyl groups of lysine (Lys) residue of gelatin. However, the $^1$H NMR spectra of pure gelatin did not show these two peaks, indicating the unmethacrylated protons of Lys (Fig. S3b). Concurrently, GelMA exhibited a spectrum at $\delta = 1.8$–1.9 ppm, indicating that the three methyl groups of the grafted methacryloyl units were absent in the pure gelatin. The resonance spectra at $\delta = 7.3$ and 7.4 ppm indicate the presence of unmethacrylated aromatic protons [3H$^+$] of phenylalanine (Phe) in both gelatin and GelMA. These results indicated the successful synthesis of GelMA for pure gelatin, which is consistent with previous reports (Geng et al., 2021; Moniruzzaman et al., 2022). For resin preparation, GelMA and PEGDA were dissolved in 1$\times$ PBS to obtain a final concentration of 0.5 wt% and 0.25 wt%, respectively. Next, the photoinitiator (0.25 %) and T-CNC@CDs were added to the solution. After mixing, the bio-resin was loaded onto the resin vat and printed using the desired structures. A schematic of the 3D printing process is shown in Fig. 2(b).

Rheological properties play a crucial role in the printability and flow consistency of bioinks while constructing high-resolution 3D structures (Ning et al., 2020). The viscoelastic properties of the developed bio-resins were evaluated using a rotational rheometer at 25 °C. A frequency sweep test (0.1 to 100 Rad s$^{-1}$) was conducted in the presence or absence of UV light (365 nm, 400 mW cm$^{-2}$). Regardless of the UV exposure, we observed an enhancement in the storage modulus (G′) and loss modulus (G″) in the presence of T-CNCs@CDs (= GPCD) compared

to the other composites (Fig. S4a). The G′ values for GM, GPD, and GPCD resins at 100 Rad s$^{-1}$ were 138, 145, and 2352 Pa, respectively. More interestingly, the G′ and G″ values for all resins were significantly higher after 30–60 s of UV irradiation. Previous studies have indicated that polymer bioinks with G′ > G″ (lower value of loss tangent) and nanofiller-induced shear-thinning property displayed suitable mechanical strength for providing the structural support for the printed structure (Garcia-Cruz et al., 2021). The enhancement in shear moduli (G′ and G″) can be explained by the fact that the uncrosslinked GPCD resin exhibited physical crosslinking through hydrogen bonding with T-CNCs@CDs as well as the higher degree of substitution of GelMA. After UV exposure, the GPCD resin immediately crosslinked via free-radical polymerization owing to the presence of LAP. Therefore, the dual crosslinking of GPCD yielded less energy dissipation during the reformation/deformation of the polymer matrix than the other resins; hence, an enhancement in G′ (G′$_{corss}$ > G′$_{uncross}$) was observed. The G′ values for the GM-, GPD-, and GPCD-crosslinked hydrogels were calculated to be 468, 2266, and 13,309 Pa, respectively (Fig. S4b). The amplitude sweep test was also conducted to understand the elasticity of the fabricated hydrogel under variable strain ranging from 0.1 to 125 %. The GPCD hydrogel showed sign of crossover ~100 % strain, where the other hydrogels were found <100 %, meaning that the incorporation of T-CNC@CDs maintained the fluidity and elasticity of the GelMA-PEGDA matrix (Fig. S4(c, d)). This was also reflected in the complex viscosity ($\eta^*$), where the crosslinked resins exhibited higher $\eta^*$ values than those of the uncrosslinked resins (Fig. 2c, d). The $\eta^*$ values of the crosslinked resins were calculated to be 1649 (GM), 3242 (GPD), and 7440 (GPCD) Pa·s at 0.1 Rad s$^{-1}$ and 10 (GM), 18 (GPD), and 134 (GPCD) Pa·s at 100 Rad s$^{-1}$. 3D printable bioinks or polymer resins must exhibit shear-thinning property during 3D printing (Highley et al., 2015). In this regard, the Power-law and Herschel-Bulkley flow model is the best-suited flow model for any printable bioink (Gao et al., 2019; Loebel et al., 2017). To evaluate the flow behavior of the developed bio-resins, the viscosity was measured at 25 °C under varying shear rates (0.1 to 100 s$^{-1}$). As shown in Fig. 2(e) and Fig. S5, the GPCD hydrogel exhibited superior shear-thinning property ($n = 0.89$, adj. R$^2$ = 0.9994) as the shear rate increased from 0.1 to 100 s$^{-1}$. The increased fluidity is probably due to the greater interaction and dynamic crosslinking of T-CNC@CDs with the GelMA/PEGDA matrix, allowing shear-induced sol-gel transition and hence, is ideal for 3D printing applications (Dutta, Hexiu, et al., 2021a; Patel et al., 2022; Zhou et al., 2019). The viscoelastic recovery of the developed bio-resins was studied using viscosity vs. time experiments with varying shear rates, where a low shear rate (0.1 s$^{-1}$) for 100 s (first interval) was initially applied to the crosslinked resins. Subsequently, the shear rate was increased to 1000 s$^{-1}$ for another 100 s (second interval), followed by a viscous recovery at 0.1 s$^{-1}$ for 100 s (third interval). As shown in Fig. 2(f), pure GM bio-resin exhibited viscosities of approximately 1309 (first interval), 0.203 (second interval), and 228 (third interval) Pa·s with a recovery strength of ~61.44 %. However, the GPD bio-resin exhibited viscosities of approximately 1334, 0.796, and 385 Pa·s, which was quite similar to the recovery strength (~70.13 %) of GM. Interestingly, the GPCD bio-resin exhibited an increase in viscosity (3161, 0.98, and 1124 Pa·s) within the measured time and shear rates, demonstrating a higher recovery strength (~74.58 %). The lower recovery strength of GM and GPD resins was probably due to the shear stress-induced destruction of physical crosslinking within the polymer chain, and therefore, the reformation occurred over a longer period (Yang et al., 2007). Next, the photorheology measurements were conducted to evaluate the change in viscosity before and after UV irradiation. The samples were exposed to UV dose (400 mW cm$^{-2}$) for approximately 30–60 s, which is similar to the 3D printing setup during DLP photo-patterning. The experimental setup is shown schematically in Fig. S6(a). As shown in Fig. S6(b), the viscosity was dramatically increased upon UV exposure in all the formulated bio-resins, with a higher change observed for the GPCD resin ($\eta_{t10} = 805$ $mPa.s \rightarrow \eta_{t100} = 1158$ $mPa.s$). This was probably due to the increased

photo-reaction at $t_{100}$ when the UV light was turned on for 30–60 s, which was sufficient for the LAP to start radical generation. However, after 100 s, the viscosity plateaued ($\eta_{t110} = 45000$ mPa.s$\rightarrow\eta_{t200} = 62050$ mPa.s$\rightarrow\eta_{t300} = 64000$ mPa.s; GPCD) owing to the completion of the photo-crosslinking reaction. As the photo-reaction is directly proportional to the root square of the concentration of photoinitiator and light intensity, higher light intensity requires an increased amount of energy to complete the reaction (O'Connell et al., 2018). The greater the degree of substitution and light intensity, the lower the time required for completing the reaction (Ouyang et al., 2020). Taken together, our results demonstrate that the formulated bio-resins are ideal for light-activated 3D printing applications with excellent shear-thinning and stress recovery properties. Digital photographs of the 3D printing and printed structures are shown in Fig. 2(g).

The structural and functional properties of the 3D printed hydrogel scaffolds were evaluated using field-emission scanning electron microscopy (FE-SEM), atomic force microscopy (AFM), cross-polarized (CP) microscopy, small angle X-ray scattering (SAXS), and differential scanning calorimetry (DSC) measurements. As shown in Fig. 3(a), the pure GM scaffolds exhibited a smaller pore distribution (pore diameter = 82 ± 13 μm) than the GPD and GPCD scaffolds at a low resolution. The GPD

scaffolds displayed anisotropic porosity (reticulate pore distribution, pore diameter = 40–120 ± 10 μm), which was further tuned to an isotropic pore distribution owing to the addition of T-CNC@CDs (=GPCD, pore diameter = 166 ± 20 μm). The horizontal and vertical line-scan profiles show the average distribution of the pore geometry in the corresponding SEM images. Interestingly, the high-resolution FE-SEM images of the cross-section showed that pure GM had a smooth surface at or near the pore surface. After the addition of PEGDA to the GelMA matrix, the pore surface appeared irregular and rough compared with that of the pure GM scaffolds. This was attributed to the greater interaction and crosslinking of GelMA with PEGDA, which facilitated the formation of a reticulate-type interconnecting polymer network. Concurrently, the GPCD scaffolds exhibited a rough geometry with layer-by-layer patterning owing to the presence of T-CNC@CDs. Nanofiller-induced self-assembly has long been explored to study the anisotropic behavior of polymer scaffolds (Ganguly et al., 2022). The self-assembly phenomenon depends on the nanofiller concentration (such as 5–20 wt%); hence, increasing the nanofiller concentration has been shown to promote the self-assembly of the polymer matrix (Ali-mohammadzadeh et al., 2022; García-Tuñon et al., 2015; Guo et al., 2022). The layer-by-layer stacking pattern in the GPCD scaffold suggests
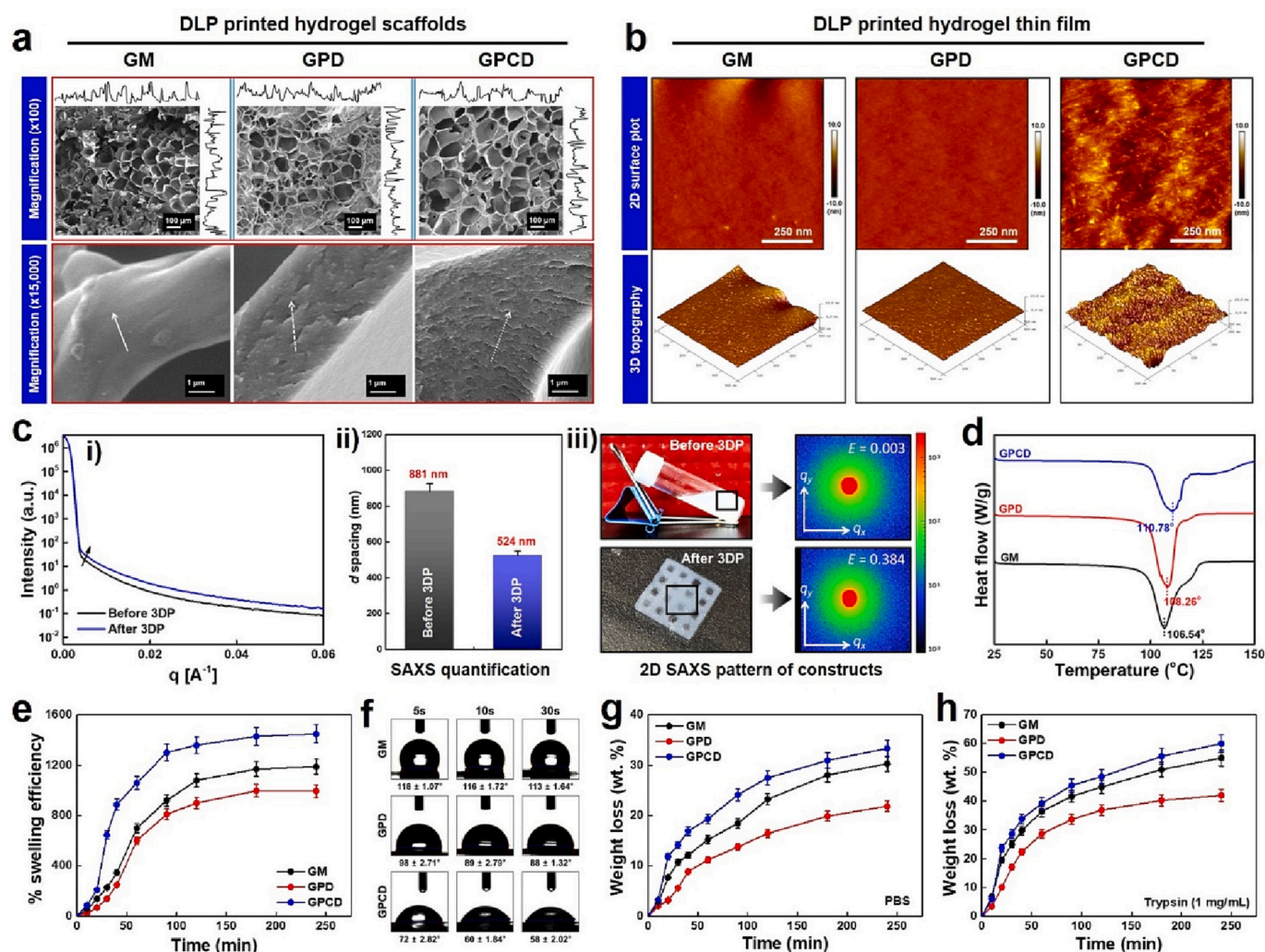


**Fig. 3.** Morphological and structural features of the fabricated hydrogel scaffolds. **(a)** FE-SEM morphology with corresponding vertical and horizontal line-scan profiles of the freeze-dried GM, GPD, and GPCD scaffolds. Scale bar: 1 and 100 μm (Mag. ×100 and ×15,000). **(b)** AFM morphology with corresponding 3D topographical images of the fabricated hydrogels showing the presence of CNC@CDs within the polymer matrix. Scale bar: 250 nm. **(c)** SAXS pattern of the liquid hydrogel resin and printed hydrogel showing the dispersion stability of the CNC-CDs (i). The *d*-spacing (ii) and 2D SAXS patterns (iii) of the corresponding resin and hydrogel. **(d)** The DSC thermograms of the GM, GPD, and GPCD hydrogels. **(e)** Swelling efficiency (%) of the developed hydrogels in PBS at 37 °C. **(f)** Water contact angle (WCA) analysis of the developed hydrogel scaffolds. **(g, h)** Degradation rate of the fabricated hydrogels in PBS and trypsin (1 mg/mL) at 37 °C.

a moderate self-assembly in the polymer matrix due to the low concentration of T-CNC@CDs (0.8 wt%).

To confirm the through mixing of GelMA and PEGDA with T-CNC@CDs, we further conducted the AFM and CP microscopy to evaluate the surface morphology and orientation of the hydrogels. The AFM phase images of GM and GPD hydrogel films exhibited nearly smooth and homogenous surface with a lowest value of root mean square (RMS) micro-roughness ($R_q$) of around 2.48 ($R_q$-GM) and 2.53 nm ($R_q$-GPD). Interestingly, the GPCD hydrogel film displayed a rough morphology ($R_q = 14.75$ nm) with a condensed peak and valley region, indicating the presence of T-CNC@CDs (Fig. 3(b)). The nanocrystals were uniformly oriented along the surface of the polymer matrix (Fig. S7(a, b)). Thus, the increased roughness form GM to GPCD (2.48 nm→14.75 nm) suggested the T-CNC@CDs-induced assembly of the polymer matrix during the drying process. The SAXS analysis was conducted before and after the 3D printing of the GPCD bio-resin to understand the molecular packing of T-CNC@CDs inside polymer matrix. The 1D SAXS graph with the corresponding 2D pattern of the liquid GPCD bio-resin exhibited a small peak around 0.0045 A$^{-1}$ owing to the local nematic phase of T-CNCs. The 3D printed GPCD hydrogel displayed a smaller peak at the same position with increased intensity (I$_{liquid}$ = 18.9 a.u. →I$_{printed}$ = 38.5 a.u.), demonstrating the local anisotropic arrangement (condensation of the local nematic islands) (Fig. 3c(i)). This was probably due to the shear-induced local alignment of T-CNC@CDs, which originated from layer-by-layer UV curing during DLP printing. The interlayer distance ($d$-spacing) of the GPCD suspension and printed hydrogel were calculated to be 881 and 524 nm (Fig. 3c(ii)), meaning that CNCs addition decreased the interlayer spacing *via* strong interaction with polymer chain and self-assembly, which is in accordance with the FE-SEM results. Based on these results, we hypothesized that T-CNC@CDs exhibited moderate self-assembly into the polymer matrix during shear-induced 3D printing, comparable to the extrusion-based self-assembly described in previous literature (Fig. 3c(iii)) (Cheng et al., 2022; Sultan & Mathew, 2018).

The chemical interactions of the developed hydrogel scaffolds were evaluated using fourier transform infra-red (FT-IR) spectroscopy. The FT-IR spectra of GM exhibited characteristic stretching vibration around 1000–2000 cm$^{-1}$ owing to the presence amide ($-NH_2$) (Huang et al., 2019) and carbonyl (C=O) moieties of GelMA (Fig. S8(a)) (Anirudhan & Mohan, 2018). The stretching vibration at approximately 3100 cm$^{-1}$ is attributed to the presence of –OH/NH$_2$ region (Amide-X) in GelMA. However, after the addition of PEGDA (=GPD scaffold), the amide-II region was slightly shifted to a lower wavenumber (1633 cm$^{-1}$→1630 cm$^{-1}$), indicating the possible occurrence of intramolecular hydrogen bonds between GelMA and PEGDA owing to the chain entanglement; the wavenumber was further shifted (1630 cm$^{-1}$ → 1629 cm$^{-1}$) after the addition of T-CNC@CDs (=GP a higher crosslinking and tougher hydrogel network was formed in the presence of PEGDA CD scaffold) (Fig. S8(b)). Since this band typically occurred owing to the photo-crosslinking reaction where $\nu$C=C was converted into C—C, the increased intensity of $\nu$C=C in the GPD and GPCD scaffolds indicated the presence of PEGDA incorporation. Similarly, the bands around 1080 cm$^{-1}$ observed for GelMA were shifted to a higher region (1095 cm$^{-1}$) in GPD because of the interaction with PEGDA and remained unchanged after the addition of T-CNC@CDs (=GPCD). Therefore, the fabricated hybrid resins displayed typical physical and photo-crosslinking reactions, consistent with previous results (Dutta, Hexiu, et al., 2021a; Wang et al., 2014).

The thermal stability of GM and its composite hydrogels was evaluated using DSC thermograms, and the results are shown in Fig. 3(d). Because all the hydrogels were dried sufficiently before DCS measurement, it was assumed that all the scaffolds were in the glassy region. Hence, there was no apparent possibility of moisture loss or a stable helix-to-coli interconnecting structure. As the temperature was increased from room temperature to higher temperatures, a noticeable thermodynamic change was observed for the endothermic peaks of the

scaffolds owing to the increased thermal motion in the polymer matrix. The transition temperature (T$_g$) values for GM, GPD, and GPCD scaffolds were calculated to be 106.54 ± 1.8 °C, 108.26 ± 2 °C, and 110.78 ± 2.4 °C, respectively. The T$_g$ value of photopolymers is profoundly affected by the degree of substitution, crosslinking, tougher nanofiller interactions, and higher molecular weight (Elkhoury et al., 2021; Kong et al., 2020). Considering this, a higher crosslinking and tougher hydrogel network was formed in the presence of PEGDA (=GPD) and was even more improved after the addition of T-CNC@CDs (=GPCD). This phenomenon was also reflected in the mechanical performance of the developed hydrogels. Fig. S9(a) shows the stress-strain curve of the hydrogel nanocomposites. The elastic modulus and toughness of the GPCD hydrogel was found to be 13.6 ± 4.2 kPa and 124 ± 5.4 kJ m$^{-3}$, significantly higher (**$p < 0.01$ and ***$p < 0.001$) than the GM and GPD hydrogels (Fig. S9(b, c)). Taken together, our results demonstrate that the addition of T-CNC@CDs into the GelMA-PEGDA matrix formed a highly interconnected, self-assembled, and thermally stable composite, which can prove to be beneficial for 3D printing and tissue engineering applications.

The scaffold morphology and gel content greatly influences the swelling behavior of the fabricated scaffolds. Gel content of the GM, GPD, and GPCD hydrogels were calculated to be ~79.12 %, ~82.78 %, and ~89.55 %, indicating that T-CNCs interaction with polymers and photo-crosslinking greatly improved the gelation. Hydrophilicity is an important factor of biomaterials for tissue engineering applications (Wang et al., 2015). The swelling properties of the fabricated hydrogel scaffolds are shown in Fig. 3(e). It was interesting to note that the GPCD scaffold exhibited a higher swelling degree (87 % →1448 %) than GM scaffold (50 %→1189 %) within a time frame of 250 min. Interestingly, all the fabricated scaffolds showed good swelling potential and reached an equilibrium state at 120 min. The higher swelling potential of the GPCD scaffold was due to the incorporation of T-CNCs@CDs, larger pores and greater surface area, which is extremely helpful for cell proliferation and differentiation (Patel et al., 2022). To understand the dynamic swelling property, we further conducted the WCA analysis and the results are displayed in Fig. 3(f). It was interesting to note that the GM and GPD hydrogel scaffold exhibited a contact angle of 118 ± 1.07° and 98 ± 2.71° after 5 s of water droplet formation. After 30s, the GM and GPD showed a contact angle of 113 ± 1.64° and 88 ± 1.32°, meaning that GPD scaffold was more hydrophilic than pure GM scaffold. However, the GPCD scaffold showed a contact angle of 58 ± 2.02° after 30s indicating its superior hydrophilicity. The origin of hydrophilic nature of the GPCD scaffold was due to the greater pore size and the presence of hydrophilic nanofiller (T-CNC@CDs), making it an ideal candidate for tissue engineering application (Dutta, Hexiu, et al., 2021a). Controlled degradation of biomaterials is important for cell migration and accumulation of the newly formed tissues (Davison et al., 2014). The degradation properties of the fabricated scaffolds were evaluated in the presence of body fluid (PBS) and proteinase (trypsin) enzyme solution, and the results are displayed in Fig. 3(g, h). As shown, the GPCD scaffold showed enhanced degradation rate than GPD and GM scaffolds in both the solutions, indicating the positive role of nanofiller (T-CNC@CDs) on biodegradation. The degradation behavior of the GM scaffold was also quite similar to the GPCD scaffold. The increased degradation rate of the GPCD scaffold was probably due to the greater insertion of fluids in the polymer matrix, thereby weakening the polymer structure and accelerate the degradation process. Patel et al. previously demonstrated that chitosan/nanocellulose scaffolds exhibited higher degradation rate owing to the structural damage of the polymer matrix (Patel et al., 2022). The higher degradation rate of the scaffolds in the presence of trypsin is due to the enzymatic degradation of GelMA, which acts as a substrate for trypsin. It is well-known that soft tissue healing, such as chronic wounds and muscle injury may take time from 2 to 3 days to months for cell migration, re-epithelialization, angiogenesis, wound closure, and tissue strengthening (Garraud et al., 2017). In this context, the developed GPCD hydrogel with ~35–48 % weight loss in 5 h

may suggest to help in initial wound healing and fibroblast recruitment *via* enhancing the inflammatory activation and extracellular matrix (ECM) formation. Taken together, our results demonstrated that the fabricated GPCD hydrogel scaffold is hydrophilic, biodegradable, and could be used as an ideal implantable material for soft tissue regeneration.

### 3.4. Study of photopolymerization kinetics and printability

Before testing the printability, we evaluated the performance of the printing resins. Generally, high-resolution 3D bioprinting can be achieved by decreasing the light penetration depth and a strong interplay between the photopolymer and photoinitiator concentration. The light penetration and curing depth can be correlated using Eq. (8):

$$C_d = D_p \times ln(E) - D_p \times ln(E_c) \qquad (8)$$

where $C_d$, $D_p$, and $E$ represent the curing depth, light-penetration depth, and irradiation dose, respectively. The light irradiation dose or intensity (*I*) depends on the distance of the light source (d) from the object, and can be defined using Eq. (9):

$$I = 1/(d)^2 \qquad (9)$$

We demonstrated the effect of the light irradiation dose as a function of distance and time to investigate the printing performance, which is quite similar to the DLP printing setup, where the *Z*-axis stage gradually moves upward after layer-by-layer printing. As illustrated in Fig. 4(a), the value of $C_d$ linearly increased (adj. $R^2 = 0.99$) as the incident dose increased for all resins. Regardless of the nanofiller, $C_d$ can also be

regulated by the light transmittance of the polymer resin (Zhao et al., 2021). Therefore, a higher polymer concentration results in a low light transmittance and high-resolution 3D printing. We observed an increase in the $C_d$ values of the GPCD resin (89*ln*E* – 332, adj. $R^2 = 0.9969$) compared to those of the GM (89*ln*E* – 227, adj. $R^2 = 0.9963$) and GPD (95*ln*E* – 238, adj. $R^2 = 0.9985$) resins. This was due to the physical crosslinking between GelMA-PEGDA and T-CNC@CDs, which facilitated strong H-bonding and decreased light transmittance. Moreover, we also observed that the GPCD resin (adj. $R^2 = 0.9956$) displayed higher $C_d$ values than the GM resin (adj. $R^2 = 0.9442$) when UV irradiation was flashed at various time points (Fig. 4(b)). Therefore, our results demonstrate that the GPCD solution is the most suitable and light-responsive among the formulated bio-resins, and can be used as an ideal material for DLP-based 3D printing.

The photopolymerization kinetics of the developed bio-resins were evaluated using real-time ATR-FTIR spectroscopy as a function of time, and the percentage of double-bond (C=C) conversion was calculated. The real-time ATR-FTIR spectra of GM and GPCD bio-resins at the indicated time points are shown in Fig. 4(c, d). In both resins, the intensity of the band at 1637 cm$^{-1}$ ($v$C=C) gradually decreased as the photopolymerization time increased from 0 to 30 s. This was due to the breakage of the C=C bonds in the photopolymers and their conversion into the C—C bonds in the presence of photopolymers. This was also confirmed by calculating the AUC value which was found to be decreased (GM$_{AUC(1637)}$ = 0.847 →0.248; GPCD$_{AUC(1637)}$ = 0.876 →0.307) after UV irradiation. The % of C=C conversion was found to be slightly higher for the GPCD resin (0 % → 68 %) than that for pure GM (0 % → 62 %) within 30 s of UV light exposure. Because the GM resin was composed of pure GelMA, adding PEGDA and T-CNC@CDs
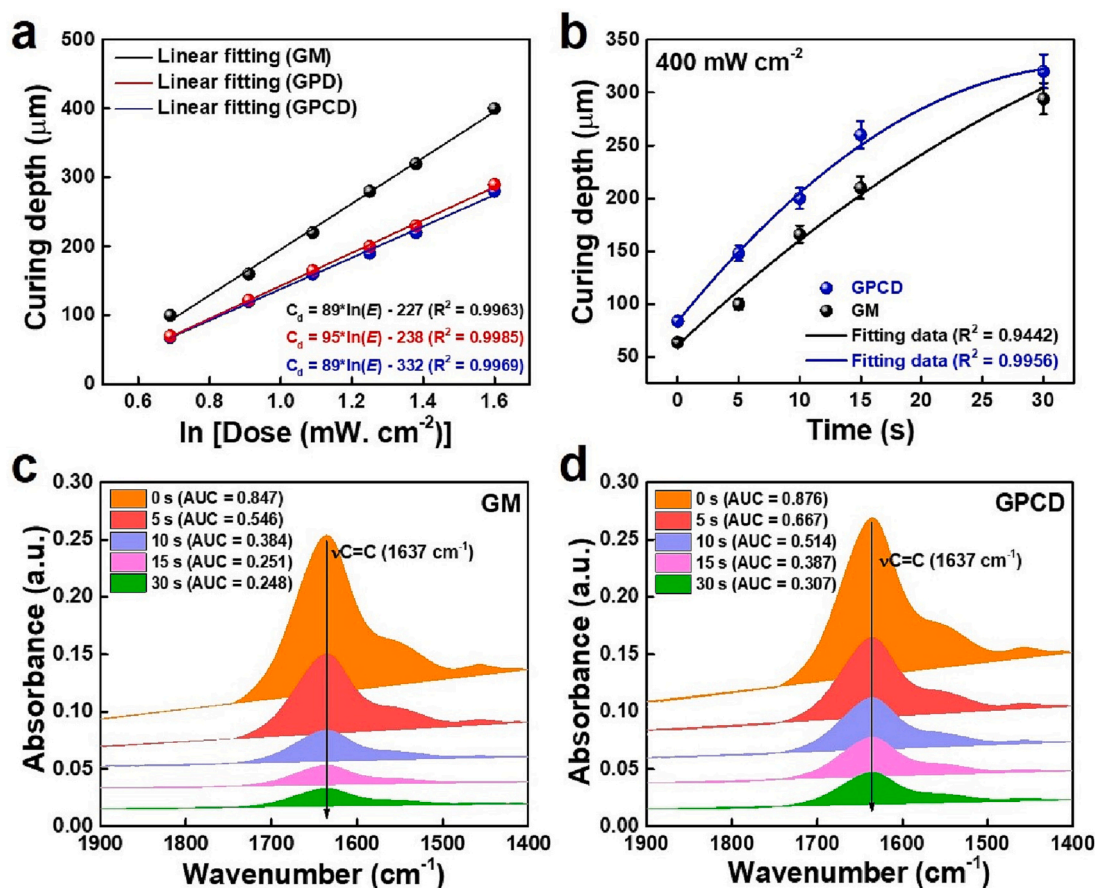


**Fig. 4.** Photopolymerization kinetics and performance of the developed bio-resins. **(a)** curing depth ($C_d$) of the GM, GPD, and GPCD bio-resins against UV irradiation dose (*E*) at 365 nm. **(b)** comparison of $C_d$ in GM and GPCD bio-resin at different time intervals after irradiation with 400 mW cm$^{-2}$ UV light irradiation. **(c, d)** ATR-FTIR spectra of the GM and GPCD bio-resins showing the photopolymerization kinetics with corresponding area under the curve (AUC) values.

decreased the viscosity of the resin, facilitating the movement of free radicals (typical radical curing) and dissolved oxygen during UV curing. After 15 s of irradiation, the % of C=C conversion underwent steady-state kinetics for both resins, indicating the completion of the photo-polymerization reaction.

Based on the excellent rheological, physicochemical, and optical properties shown by GPCD resin in the present study, we chose this resin for 3D printing. The 3D printing workflow is schematically shown in Fig. 5(a). To test printability and fluorescence property, we designed various CAD structures with varying infill densities. We tested the 3D printing of a square lattice, a hexagonal lattice (3, 4, and 6 hexagons), small vascular tree patterns, and hollow cylindrical structures (Fig. 5 (b)). Each structure was separated based on the number of layers such as 20- and 40-layered structures. The thickness of each layer was designed to be 0.1 mm (100 μm). Therefore, the stunt heights of the 20- and 40-layer structures were 2 and 4 mm, respectively. Fig. 5(c) shows the successful 3D printing of various structures. The printed hydrogels exhibited strong fluorescence under 365 nm UV light owing to the presence of T-CNC@CDs. We observed a nearly uniform height for the printed structures when compared to the theoretical height. Interestingly, the 20-layered structure exhibited a superior printing resolution with uniform porosity. However, the 40-layered structure exhibited a

slightly lower printing quality owing to the closure of the pores between the strands. This was probably due to the excess accumulation of resins inside the pores, resulting in self-polymerization during UV curing. The enlarged images of the 3D printed hydrogels are shown in Fig. S10(a, b). Next, we printed some of the biomimetic tissue structures, such as the blood vessel (50 layers), muscle (30 layers), full-thickness skin (30 layers), and ear (200 layers) prototypes based on the CAD model (Fig. 6 (a)). We successfully printed the aforementioned structures (Fig. 6(b)) without any structural disturbances (cylinder, muscle, and skin model). However, the ear model did not actually recapitulate the original CAD structure after 300 layers of printing. The optical microscopy images revealed that all the printed structures exhibited smooth morphology at or near the strands or the edges (Fig. S11). The printing accuracy of the tested models also revealed that cylindrical and ear model had low printing resolution in x-y axis; however, no such differences were found in the z-axis resolution (Fig. 6(c)). The printing resolution was also correlated with the mechanical property of the hydrogels. As depicted in Fig. 6(d), the ear model exhibited higher compressive strength than other models. Desired printing structure with proper mechanical support is one of the crucial factors for organ-specific tissue engineering. Therefore, we hypothesized that the formulated GPCD bio-resin can only print small-scale objects with high resolution and is best suited for
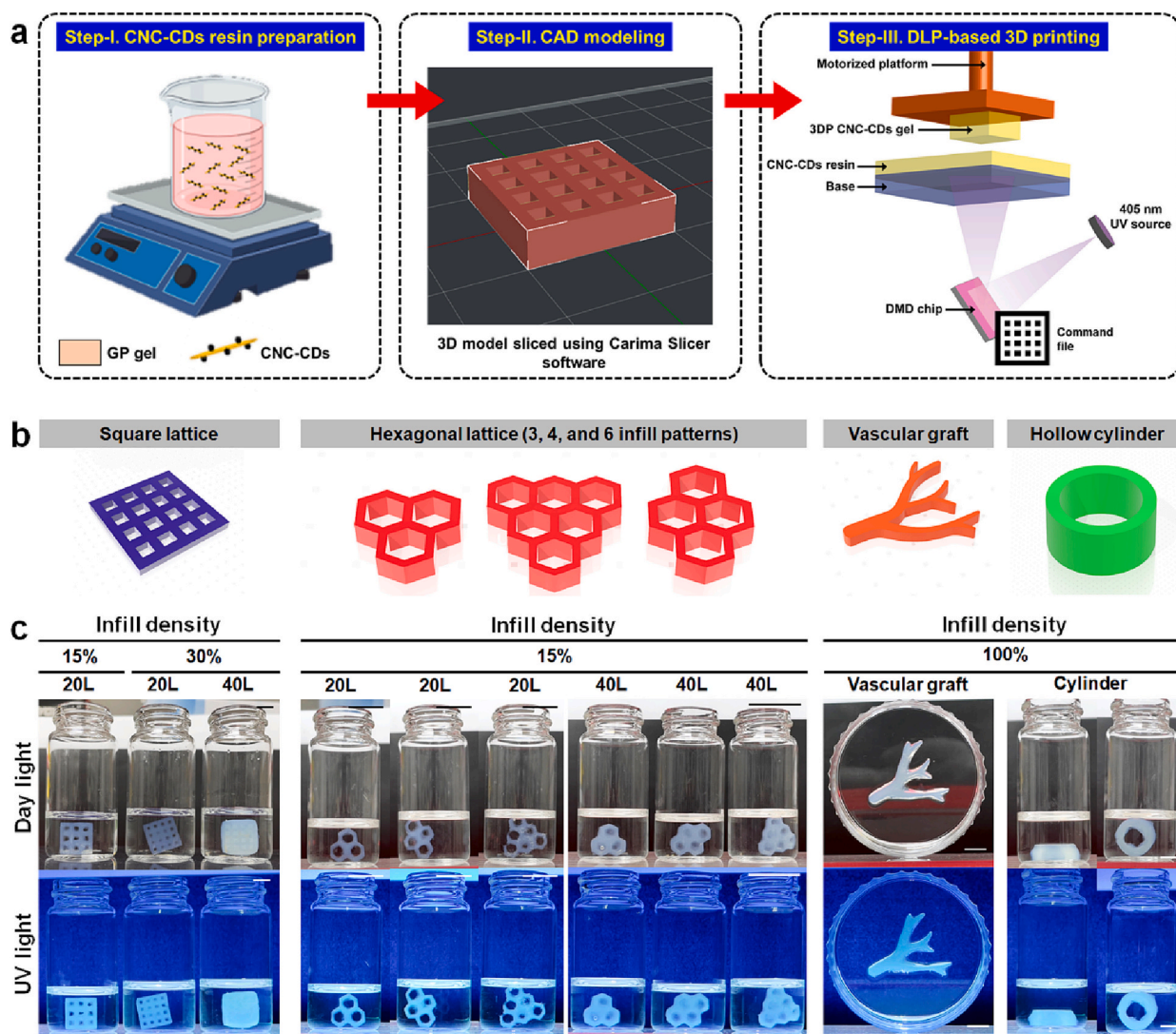


**Fig. 5.** 3D printing of GPCD bio-resin. **(a)** Schematic illustration of the resin preparation, CAD modeling, and 3D printing process using the GPCD bio-resin. **(b)** CAD model of the target structures with various lattice components (square, hexagonal, vascular graft, and hollow cylinder). **(c)** Digital photographs of the 3D printed GPCD hydrogels under visible and UV light indicating the fluorescence nature of the hydrogels. Scale bar: 5 mm.
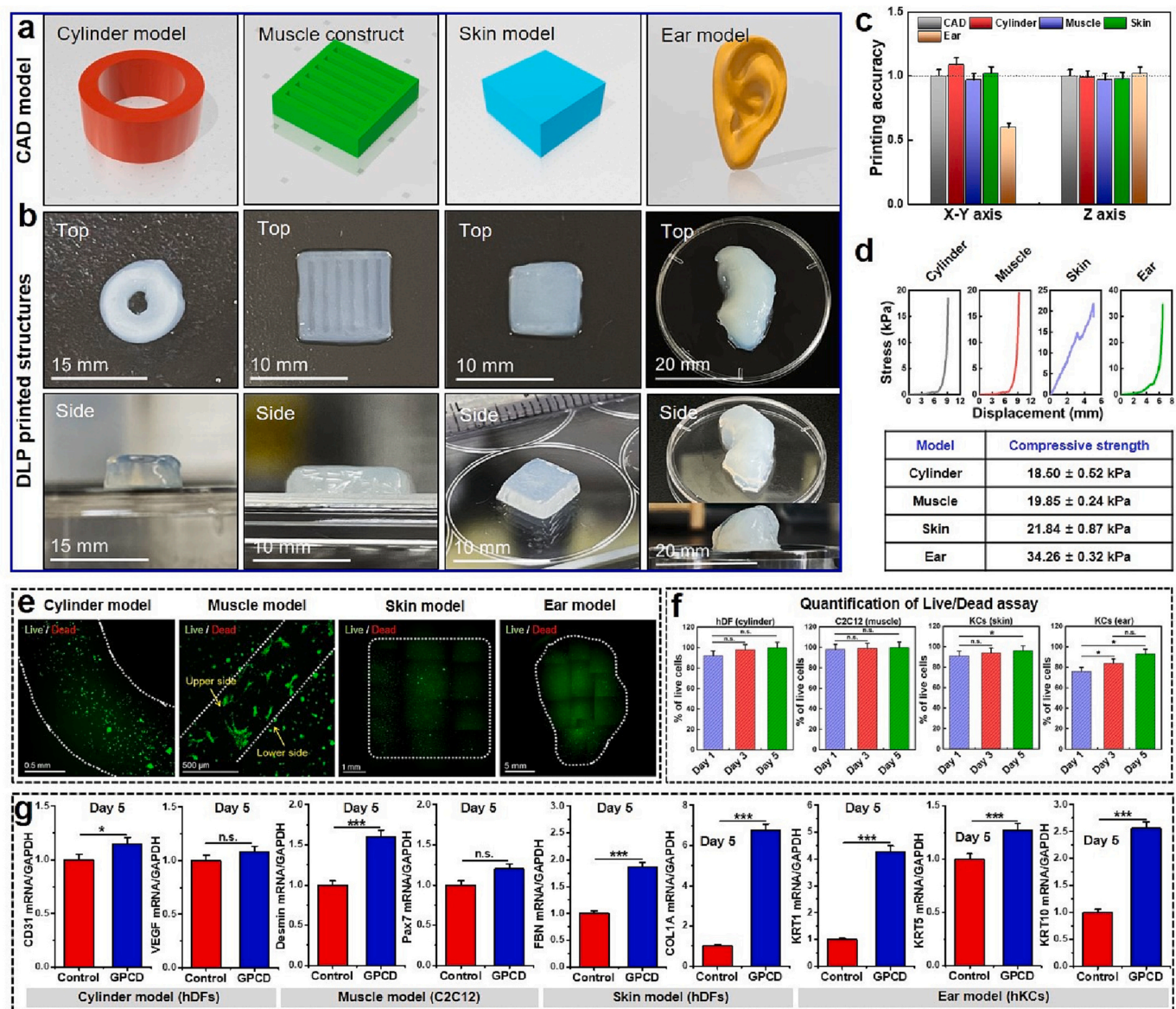
**Fig. 6.** DLP printing of model structures and assessment of *in vitro* biocompatibility using GPCD bio-resin. **(a)** The CAD model of the target constructs used in this study. **(b)** Digital photographs of the printed constructs. Scale bar: 10, 15, and 20 mm. **(c)** Printing accuracy of the developed constructs w.r.t. CAD models. **(d)** Representative compressive strength results of the developed hydrogel constructs. **(e, f)** Biocompatibility assessment of the human keratinocytes (KCs), human dermal fibroblast (hDFs), and mouse myoblast (C2C12) in the presence of 3D printed GPCD hydrogels after 5 days of incubation with corresponding live/dead quantification data. Scale bar: 500 μm, 0.5 mm, 1 mm, and 5 mm. **(g)** qRT-PCR gene expression results of the differentiated hDFs (*CD31*, *VEGF*, *FBN*, and *COL1A*), C2C12 (*Desmin* and *Pax7*), and hKCs (*KRT1*, *KRT5*, and *KRT10*) in the presence of GPCD hydrogel after 5 days of culture. Data are mean ± s.d. of triplicate ($n = 3$) experiments, statistical significance at *$p < 0.05$ and ***$p < 0.001$ (n.s. = not significant).

micro-tissue engineering.

We also tested the cytocompatibility of the 3D printed prototypes using human and mouse cell lines. The cells were cultured on printed prototypes and incubated for 5 days. The Live/Dead assay was conducted to evaluate the cytotoxicity (Fig. 6(e)). Interestingly, the FL images showed that none of the printed hydrogels were toxic to hDFs, human keratinocytes (hKCs), or murine myofibroblasts (C2C12) cells after 3 days of culture, indicating the superior biocompatibility of the developed hydrogels. The viability of the hDFs, C2C12, and KCs after 5 days of incubation were calculated to be ~98 %, 99 %, and 96 %, respectively (Fig. 6(f)). The WST-8 assay also showed an enhancement in the viability of hDFs after 7 days of cell culture, which also confirmed the biocompatible nature of the hydrogels (Fig. S12). Based on the outstanding biocompatibility, we next evaluated the differentiation potential of the cultured cells. The cell differentiation capability was

evaluated using qRT-PCR analysis after 5 days of treatment and the results are shown in Fig. 6(g). It was interesting to note that the hDFs cultured in EGM/GPCD hydrogel (cylinder model) exhibited higher expression (*$p < 0.05$) of endothelial gene markers, CD31 (~1.5 fold) and VEGF (~1.08 fold) than control. Moreover, the hDFs incubated with DMEM-F12/GPCD hydrogel (skin model) significantly (***$p < 0.001$) elevated the fibroblastic gene markers expression, *FBN* (~1.86 fold) and *COL1A* (~6.74 fold), respectively. Similarly, the hKCs (ear model) also exhibited an enhanced expression (***$p < 0.001$) of *KRT1* (~4.27 fold), *KRT5* (~1.27 fold), and *KRT10* (~2.56 fold) markers compared to control, suggesting that the fabricated hydrogel is capability of cell proliferation and differentiation. There results were in accordance with our previous reports where CNCs-containing scaffolds has been shown to promote differentiation of fibroblasts and keratinocytes (Ganguly et al., 2022). Additionally, the C2C12 cells also exhibited an elevated

expression of myoblastic gene marker, *Desmin* up to 1.64 fold (\*\*\**p* < 0.001) than control, suggesting that the fabricated construct is efficient for controlling the myogenesis. It is well-known that hydrogel porosity, wettability, surface stiffness, and biopolymer composition played crucial role in cell adhesion and differentiation (Dutta et al., 2023a; Jenkins & Little, 2019). In agreement with previous reports, the fabricated GPCD hydrogel with superior hydrophilicity, desired porosity, and presence of cell-adhesive peptides are the reason for greater adhesion and differentiation of hDFs, C2C2, and hKCs. Taken together, our results suggest that the fabricated GPCD bio-resin is printable, biocompatible, and could be used for generating micro-tissue models for tissue engineering.

### 3.5. Evaluation of in vitro imaging ability of GPCD hydrogel

It is well-known that when the fluorescent compounds were mixed with polymer solution to prepared glowing hydrogel, the system pH as well as hydrogel composition significantly affect the emission behavior of the hydrogel (Kim et al., 2020). To understand the fluorescence stability under various biological conditions, we printed the GPCD hydrogels (5 × 5 mm) using the DLP printer based on the CAD model (Fig. 7a (i)). The printed hydrogel disc was immersed into various pH buffer (6.5, 7.4, and 9.5) at 37 °C under mild shaking (150 rpm) to evaluate the fluorescence stability (Fig. 7a(ii)). The wide range of pH stability of a

fluorophore is highly suitable for implantation in both healthy tissue (pH 7.4) as well as cancerous tissue (pH 6.2–6.6) for tracking analysis (Dutta et al., 2022). The pure GelMA (GM) was also taken as control group. As illustrated in Fig. 7(b), the GM hydrogel exhibited a faint fluorescent signal under excitation of 405 nm in the presence of various pH buffers, suggesting the moderate auto-fluorescence nature of GM. On the other hand, the GPCD hydrogel exhibited strong blue emission under various pH buffer even after incubation for one month (Fig. 7c). Thus, the origin of strong blue fluorescence in the GPCD hydrogel was due to the addition of T-CNC@CDs and not for the GelMA or T-CNCs alone (Fig. S13). The time-dependent fluorescence intensity of the GPCD hydrogel was measured using the PL spectrophotometer and the data was normalized to fluorescence of the GM hydrogel. Interestingly, the GPCD hydrogels displayed strong fluorescence retention property under various pH buffers. The fluorescence retention of GPCD hydrogel under pH 6.5, 7.4, and 9.5 were calculated to be ~87.91 %, ~89.2 %, and ~84.6 %, respectively. These results suggest that the fabricated hydrogel could be used as an implantable material for long-term non-invasive tracking analysis. The normalized PL intensity of the GPCD hydrogel after one-month incubation is given in Fig. 7(d).
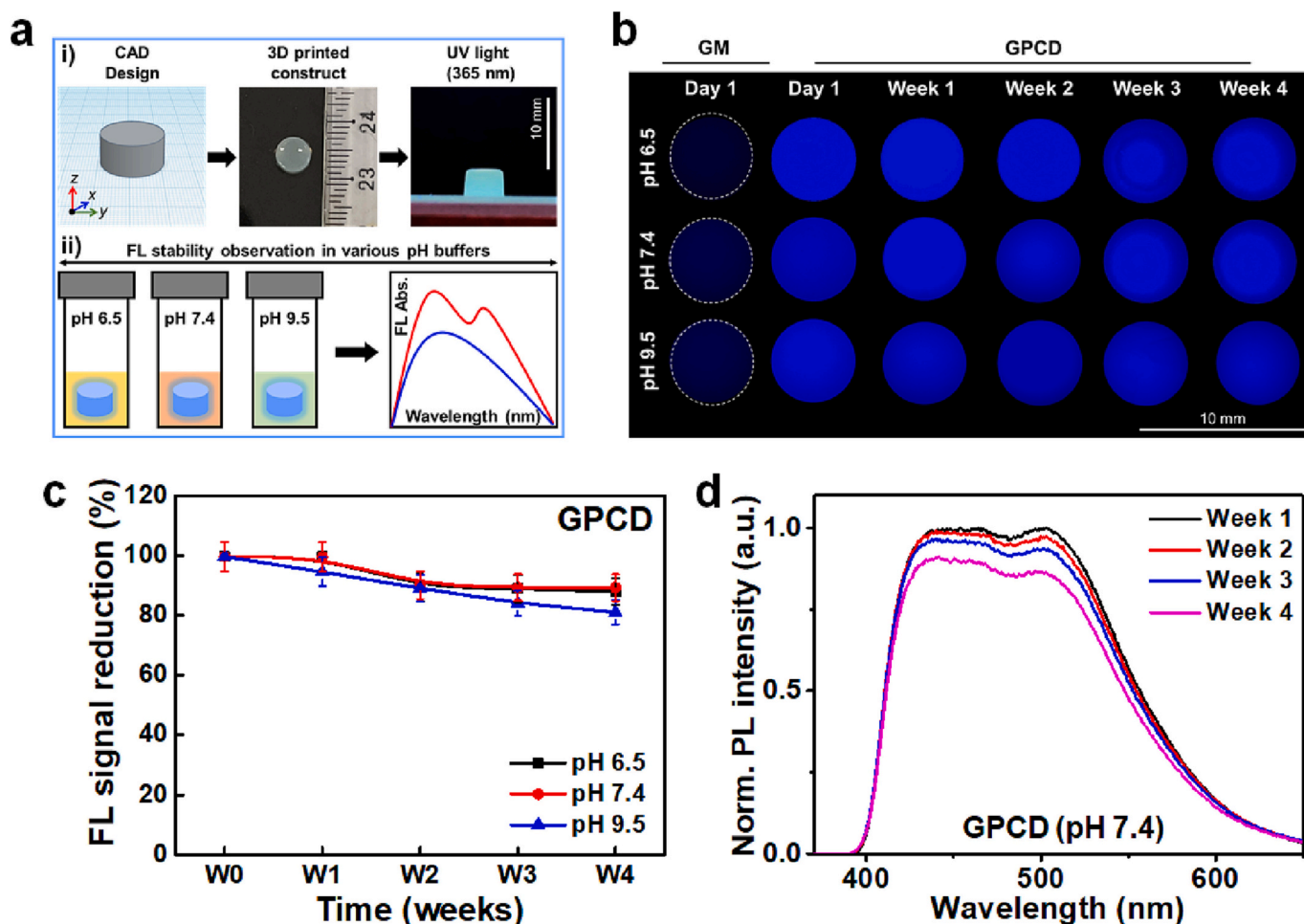


**Fig. 7.** Demonstration of the fluorescence stability of the GPCD hydrogel. **(a)** The GPCD hydrogel was printed according to the CAD model and visualized using 365 nm UV illuminator (i). The GPCD hydrogels were immersed in various pH buffer to evaluate the fluorescence stability up to one month (ii). **(b)** *In vitro* imaging of the 3D printed GPCD hydrogels after incubation in various pH buffers at indicated time points. The GM hydrogels were taken as control. **(c)** Quantification of the fluorescence intensity of the GPCD hydrogels at indicated time points. **(d)** Normalized PL intensity of the GPCD hydrogels in pH 7.4 after one month of incubation. Scale bar: 10 mm.

### 3.6. 3D bioprinting of proof of concept model and image-guided tissue regeneration

The excellent printability and improved biocompatibility of the GPCD bio-resin motivated us to scrutinize the bioprinting of small tissue-like structures. As a *proof of concept*, we bioprinted full-thickness skin and blood vessel prototypes to recapitulate the native tissue structure. As illustrated in Fig. 8(a), hDFs (approximately $2.5 \times 10^5$) were mixed
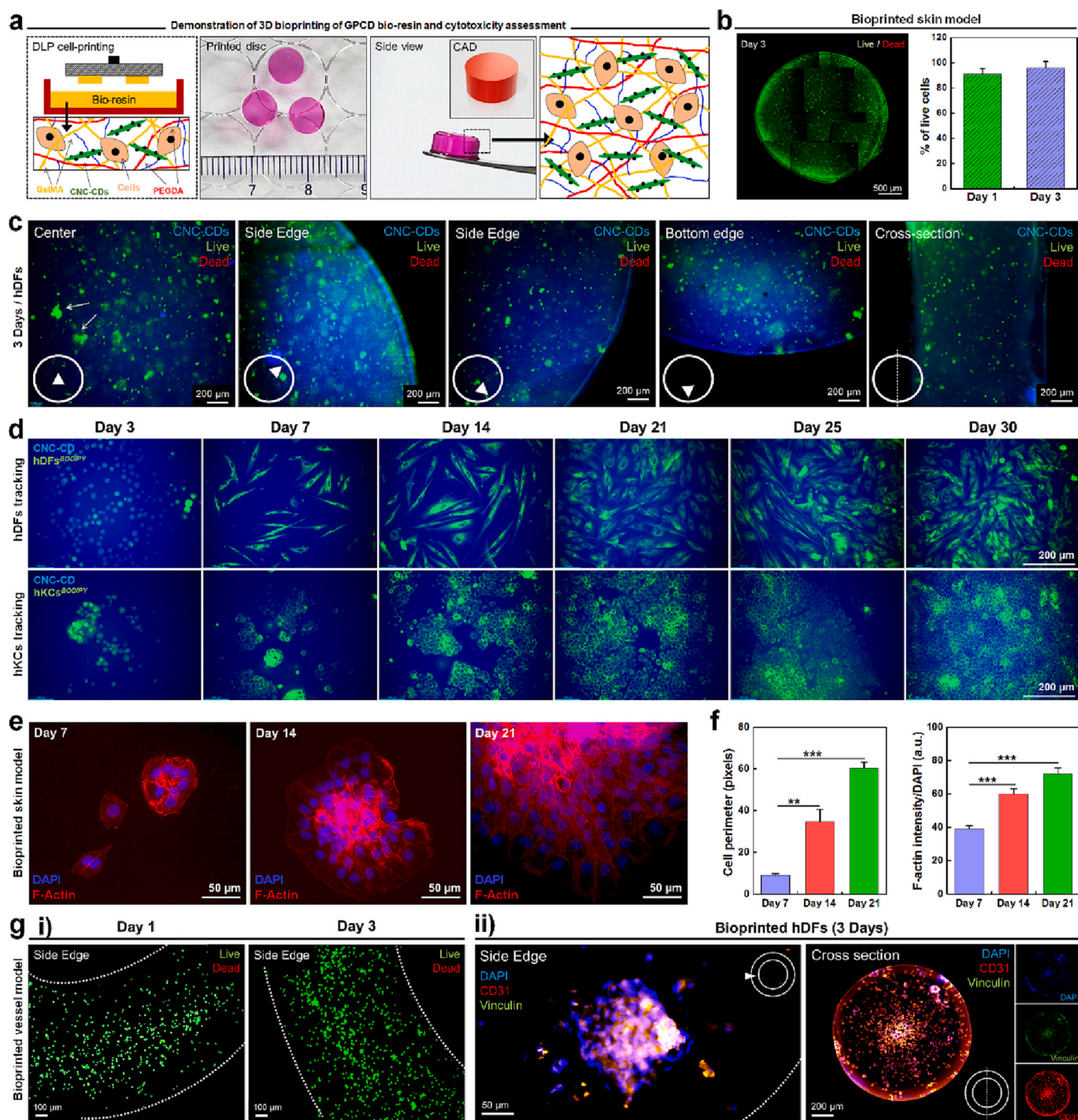


**Fig. 8.** 3D bioprinting of 'proof-of-concept' models using GPCD bio-resin and dynamic cell tracking. **(a)** Schematic illustration of the bioprinting process. The cells were mixed with the GPCD bio-resin and loaded onto the resin vat and precisely printed. **(b)** Representative Live/Dead imaging with quantification data of a full-thickness skin model using hDFs after 3 days of incubation. The random images were taken from each side of the hydrogel disc to reconstruct the full image. **(c)** FL microscopy images of the hDFs at various points as indicated. The hydrogel surface was stained blue due to the presence of T-CNC@CDs. Insets indicate the position of the cells inside the hydrogel. **(d)** Dynamic tracking of hDFs and hKCs inside bioprinted hydrogel up to 30 days. **(e)** F-actin morphology of the hKCs inside bioprinted hydrogel at indicated time points. **(f)** Semi-quantitative analysis of the cell perimeter and F-actin distribution of hKCs. **(g)** 3D bioprinting of a blood vessel prototype using hDFs showing the viable cells (i). Representative FL images of the surface and cross-sectional view (ii) of the hydrogel showing the presence of CD31 positive hDFs (red). The cytoskeletal proteins were stained with vinculin (green), and nucleus was stained with DAPI (blue). Scale bar: 50, 100, 200, and 500 µm. Data are mean ± s.d. of triplicate (n = 3) experiments, statistical significance at **$p < 0.01$ and ***$p < 0.001$.

**Table 1**

A comparative table showing the use and application of various fluorescent resins for tissue engineering.

| Nanofiller | Resin composition | Optical properties | Application | References |
|---|---|---|---|---|
| Cellulose nanocrystals (CNCs) | Polyethylene glycol diacrylate (PEGDA) + glycerol-1,3-diglycerolate diacrylate (DiGlyDA) + CNCs (0.2–5 wt%) | N/A | N/A | (Li et al., 2019) |
| Cellulose nanocrystals (CNCs) | Commercial resin (DC-36) + nanoclay + CNCs (0.25 wt%) | N/A | N/A | (Bae & Kim, 2021) |
| Cellulose nanofibrils (CNFs) | Polyurethane (PU) + reduced graphene oxide (rGO) + polyethylene glycol (PEG, 0.5 wt%) + CNFs (0.25–1 wt%) | N/A | N/A | (Mohan et al., 2019) |
| N/A | Itaconic acid + glycerol + vanillic acid + 1,3-propanediol | Phosphorescence | Skin tissue engineering | (Maturi et al., 2020) |
| Silk fibroin | Methacrylated silk fibroin (SilMA, 20 % $w/v$) + green fluorescent protein (GFP) | Fluorescence | 3D bioprinting of fibroblast cells | (Lee et al., 2022) |
| CdSe quantum dots (QDs) | Tris(2-hydroxyethyl) isocyanurate acrylate + ethoxylated (6) trimethylpropane triacrylate + CdSe QDs | Fluorescence | N/A | (Jaiswal et al., 2021) |
| Carboxymethyl cellulose (CMC) | Methacrylated CMC (M-CMC, 20 mg/ mL) | N/A | 3D printing and fibroblast cell culture | (Melilli et al., 2020) |
| Carbon dots-modified TEMPO-CNCs (T-CNC@CDs) | Gelatin methacrylate (GelMA, 0.5 wt%) + PEGDA (0.1 wt %) + T-CNC@CDs (0.8 wt%) | Fluorescence | 3D printing and bioprinting of fibroblast and keratinocyte cells- soft tissue engineering | This study |

with GPCD bio-resin and gently mixed by pipetting. Next, the hDF-encapsulated resin was incubated at $37 \pm 2$ °C for 30 min and loaded onto the resin vat. Next, a $5 \times 2$ mm (printing resolution of 100 μm) circular construct was carefully printed in a sterile environment with an average printing time of 5 to 8 min. The small construct was printed to minimize the printing time and maximize the viability of hDFs. The hDF-laden 3D bioprinted hydrogels were then incubated with DMEM/F-12 medium to promote rapid proliferation. For the blood vessel prototype, the hDFs-laden bio-resin was printed using a hollow tube model with a ring diameter of 0.1 mm (~100 μm). Next, the vascular graft model was incubated in an angiogenic induction medium as described by Newman et al. (2011).

Viability of the bioprinted skin and blood vessel prototypes was assessed using the Live/Dead staining assay. Interestingly, hDFs grew properly within the printed GPCD hydrogel, and the 3D bioprinting process was non-toxic for these hDFs. No noticeable damage or dead cells were observed after 3 days of hDF culture. The hDFs were appeared round or aggregated within the bioprinted construct after 3 days of culture. A reconstructed image of the skin prototype with hDF cells is shown in Fig. 8(b). The proliferation rate of the hDFs after 3 days was calculated to be ~97.64 %, which is consistent with the previously reported GelMA-based hydrogels (Wang et al., 2015; Xie et al., 2022; Ying et al., 2018). Next, we examined the tracking ability of the cells inside the bioprinted hydrogels using fluorescence microscopy. As illustrated in Fig. 8(c), the GPCD hydrogel emitted blue fluorescence under excitation at $\lambda = 405$ nm owing to the presence of T-CNC@CDs. The images of the live (AO/green) and dead (EtBr/red) cells were merged with the corresponding GPCD hydrogel image to obtain a hybrid merged image. Strikingly, the central region of the hydrogel exhibited a significantly (*$p < 0.05$) larger cell aggregations (~$98 \pm 5$ μm) than that at the side (~$30 \pm 5$ μm) or bottom edge (~$48 \pm 5$ μm) of skin constructs. The insets show the position of the cells inside the hydrogel. These results suggest that the hDFs mainly aggregated into the central region of the bioprinted constructs and therefore formed larger cell aggregates. The possible reason for round/aggregated cells inside the bioprinted hydrogel was due to the greater pore size and highly cross-linked polymeric structure. Usually, the bioprinted cells slowly proliferate immediately after printing owing to the shear stress and the less availability of nutrients. As the incubation time increased and the hydrogel started swelling, the bioprinted cells had greater access to the nutrients and dissolved oxygen (Dutta et al., 2023b; Jia et al., 2016). The cross-sectional morphology of the bioprinted construct also showed homogenous cell distribution inside the hydrogel. To track the bioprinted cells for longer time, we also performed the imaging experiment up to 30 days (one month) using bioprinted hDFs and hKCs. The cells were pre-labeled with CellTracker Green dye (excitation/emission = 492/517 nm) to

visualize easily under FL microscope. As shown in Fig. 8(d), the cells appeared round/aggregated at day 3. From day 7 onwards, the hDFs exhibited typical oval/spindle-shaped morphology at day 7 and day 14. At day 25 onwards, the whole area of the GPCD was covered with the hDFs. A similar trend was also noticed in case of hKCs. Note that the cell coverage was significantly higher in hKCs than the hDFs, since hKCs grew in colony. Thus, the GPCD hydrogel can be used to track the growth and movement of human cells which have potential use in non-invasive wound management and disease monitoring.

Next, we observed the morphology of the bioprinted hKCs after 3 weeks of culture using F-actin probe. As demonstrated in Fig. 8(e), the hKCs appeared in colony after 7 days with regular arrangement of F-actin (red) and nucleus (green). As the colony started to grow (2–3 weeks), the cell perimeter and actin intensity was significantly increased (***$p < 0.001$) owing to the increase of cell mass (Fig. 8(f)). The bioprinted vascular graft displayed a similar pattern of cell growth, with a higher cell population in the center and a lower population at the edges (Fig. 8g(i)). The hDFs were stained with the angiogenic marker CD31 after 7 days of angiogenic induction to examine angiogenic potential. As shown in Fig. 8g(ii), the bioprinted hDFs were positive for CD31 (red), with cytoplasmic localization of vinculin (green). Similarly, a cross-section through the vascular ring showed that CD31$^+$ cells mainly gathered toward the central region of the bioprinted hydrogel. The insets show the position of the cells in in bioprinted structure. Based on these results, we envisage that the bioprinted prototypes are non-toxic to hDFs and hKCs, trackable, promote rapid proliferation, and help in recapitulating the native microenvironment of the human tissues. A comparative study describing the importance of various 3D printed fluorescence hydrogels and their applications in tissue engineering is presented in Table 1.

## 4. Conclusion

In summary, using an eco-friendly approach, we successfully synthesized a polysaccharide-tagged fluorescent probe (T-CNC@CDs) and utilized it for DLP printing. The 3D bioprinting of low-concentration resin with tunable mechanical properties and desirable biocompatibility holds great promise for tissue engineering. However, an entirely bio-based and high-resolution printing strategy remains challenging owing to the low availability of bio-based resins. Herein, for the first time, we have demonstrated an ultra-low-concentration polymeric bio-resin with tunable optical properties and enhanced physicochemical properties. The bio-resin was fabricated using GelMA and PEGDA, and was photopolymerized to form high-resolution print constructs to improve printability. T-CNC@CD-reinforced bio-resin (*i.e.*, GPCD) is highly fluorescent, electrochemically active, exhibits desirable

rheological properties, and is printable at room temperature. We demonstrated 3D printing of simple and small geometrical structures without deformation by applying various optimizations. However, one of the significant challenge of the present study is that high-resolution bulk printing is quite difficult to achieve owing to the radial curing of the bio-resin solution and the low concentration of the T-CNC@CDs. The 3D printed biological constructs exhibited higher cell proliferation capabilities (viability ~98 %) and induced the differentiation of hDFs (*CD31*, *VEGF*, *FBN*, and *COL1A*), C2C12 (*Desmin* and *Pax7*), and hKCs (*KRT*). Additionally, bioprinting was performed using hDFs to print full-thickness skin and blood vessels as a *proof of concept*. Our results show that bioprinted *in vitro* models can recapitulate the native microenvironment of the skin and blood vessels without any loss or damage to the printed constructs with long-time tracking ability. This study will help in establishing an intelligent platform for designing next-generation glowing hydrogels that can be synthesized with minimal efforts and image-guided tissue regeneration studies. We expected application possibilities in tissue engineering, especially in development of microtissues to enable real-time monitoring of cell migration and differentiation for clinical practice.

## CRediT authorship contribution statement

**Sayan Deb Dutta:** Conceptualization, Methodology, Validation, Formal analysis, Data curation, Writing – original draft, Writing – review & editing, Visualization, Supervision, Project administration. **Tejal V. Patil:** Formal analysis, Methodology, Data curation. **Keya Ganguly:** Formal analysis, Methodology, Data curation, Writing – review & editing. **Aayushi Randhawa:** Formal analysis, Software, Validation. **Rumi Acharya:** Formal analysis, Validation. **Md Moniruzzaman:** Writing – review & editing, Visualization, Supervision, Project administration. **Ki-Taek Lim:** Writing – review & editing, Visualization, Supervision, Project administration, Funding acquisition.

## Declaration of competing interest

The authors declare no competing financial interests.

## Data availability

Data will be made available on request.

## Acknowledgments

## Appendix A. Supplementary data

Supplementary data to this article can be found online at https://doi.org/10.1016/j.carbpol.2023.121232.

## References

Alimohammadzadeh, R., Rafi, A. A., Goclik, L., Tai, C.-W., & Cordova, A. (2022). Direct organocatalytic thioglycolic acid esterification of cellulose nanocrystals: A simple entry to click chemistry on the surface of nanocellulose. *Carbohydrate Polymer Technologies and Applications, 3*, Article 100205.

Anirudhan, T. S., & Mohan, A. M. (2018). Novel pH sensitive dual drug loaded-gelatin methacrylate/methacrylic acid hydrogel for the controlled release of antibiotics. *International Journal of Biological Macromolecules, 110*, 167–178.

Bae, S.-U., & Kim, B.-J. (2021). Effects of cellulose nanocrystal and inorganic nanofillers on the morphological and mechanical properties of digital light processing (DLP) 3D-printed photopolymer composites. *Applied Sciences, 11*, 6835.

Bhatt, M., Bhatt, S., Vyas, G., Raval, I. H., Haldar, S., & Paul, P. (2020). Water-dispersible fluorescent carbon dots as bioimaging agents and probes for Hg2+ and Cu2+ ions. *ACS Applied Nano Materials, 3*, 7096–7104.

Bose, S., Koski, C., & Vu, A. A. (2020). Additive manufacturing of natural biopolymers and composites for bone tissue engineering. *Materials Horizons, 7*, 2011–2027.

Boyle, B. M., French, T. A., Pearson, R. M., McCarthy, B. G., & Miyake, G. M. (2017). Structural color for additive manufacturing: 3D-printed photonic crystals from block copolymers. *ACS Nano, 11*, 3052–3058.

Camposeo, A., Persano, L., Farsari, M., & Pisignano, D. (2019). Additive manufacturing: Applications and directions in photonics and optoelectronics. *Advanced Optical Materials, 7*, Article 1800419.

Cesewski, E., Haring, A. P., Tong, Y., Singh, M., Thakur, R., Laheri, S., et al. (2018). Additive manufacturing of three-dimensional (3D) microfluidic-based microelectromechanical systems (MEMS) for acoustofluidic applications. *Lab on a Chip, 18*, 2087–2098.

Chan, J. Y. E., Ruan, Q., Jiang, M., Wang, H., Wang, H., Zhang, W., et al. (2021). High-resolution light field prints by nanoscale 3D printing. *Nature Communications, 12*, 1–9.

Cheng, F., Liu, C., Wei, X., Yan, T., Li, H., He, J., et al. (2017). Preparation and characterization of 2, 2, 6, 6-tetramethylpiperidine-1-oxyl (TEMPO)-oxidized cellulose nanocrystal/alginate biodegradable composite dressing for hemostasis applications. *ACS Sustainable Chemistry & Engineering, 5*, 3819–3828.

Cheng, Q., Guo, J., Cao, X., & Chang, C. (2022). The digital printing of chromatic pattern with a single cellulose nanocrystal ink. *Chemical Engineering Journal, 439*, Article 135670.

Chizari, S., Shaw, L. A., & Hopkins, J. B. (2019). Simultaneous printing and deformation of microsystems via two-photon lithography and holographic optical tweezers. *Materials Horizons, 6*, 350–355.

Choi, H. S., & Kim, H. K. (2020). Multispectral image-guided surgery in patients. *Nature Biomedical Engineering, 4*, 245–246.

Cohen, N., Ochbaum, G., Levi-Kalisman, Y., Bitton, R., & Yerushalmi-Rozen, R. (2019). Polymer-induced modification of cellulose nanocrystal assemblies in aqueous suspensions. *ACS Applied Polymer Materials, 2*, 732–740.

Cometta, S., Jones, R. T., Juárez-Saldivar, A., Donose, B. C., Yasir, M., Bock, N., et al. (2022). Melimine-modified 3D-printed polycaprolactone scaffolds for the prevention of biofilm-related biomaterial infections. *ACS Nano, 16*, 16497–16512.

Dai, B., Zhang, L., Zhao, C., Bachman, H., Becker, R., Mai, J., et al. (2021). Biomimetic apposition compound eye fabricated using microfluidic-assisted 3D printing. *Nature Communications, 12*, 1–11.

Davison, N. L., Barrère-de Groot, F., & Grijpma, D. W. (2014). Degradation of biomaterials. *Tissue Engineering*, 177–215.

Đorđević, L., Arcudi, F., Cacioppo, M., & Prato, M. (2022). A multifunctional chemical toolbox to design carbon dots for biomedical and energy applications. *Nature Nanotechnology, 17*, 112–130.

Drury, J. L., & Mooney, D. J. (2003). Hydrogels for tissue engineering: Scaffold design variables and applications. *Biomaterials, 24*, 4337–4351.

Dutta, S. D., Bin, J., Ganguly, K., Patel, D. K., & Lim, K.-T. (2021c). Electromagnetic field-assisted cell-laden 3D printed poloxamer-407 hydrogel for enhanced osteogenesis. *RSC Advances, 11*, 20342–20354.

Dutta, S. D., Ganguly, K., Randhawa, A., Patil, T. V., Patel, D. K., & Lim, K.-T. (2023a). Electrically stimulated 3D bioprinting of gelatin-polypyrrole hydrogel with dynamic semi-IPN network induces osteogenesis via collective signaling and immunopolarization. *Biomaterials, 294*, Article 121999.

Dutta, S. D., Ganguly, K., Randhawa, A., Patil, T., Patel, D. K., & Lim, K.-T. (2023b). Electrically stimulated 3D bioprinting of gelatin-polypyrrole hydrogel with dynamic semi-IPN network induces osteogenesis via collective signaling and immunopolarization. *Biomaterials, 294*, 1–20, 121999.

Dutta, S. D., Hexiu, J., Kim, J., Sarkar, S., Mondal, J., An, J. M., et al. (2022). Two-photon excitable membrane targeting polyphenolic carbon dots for long-term imaging and pH-responsive chemotherapeutic drug delivery for synergistic tumor therapy. *Biomaterials Science, 10*, 1680–1696.

Dutta, S. D., Hexiu, J., Patel, D. K., Ganguly, K., & Lim, K.-T. (2021a). 3D-printed bioactive and biodegradable hydrogel scaffolds of alginate/gelatin/cellulose nanocrystals for tissue engineering. *International Journal of Biological Macromolecules, 167*, 644–658.

Dutta, S. D., Patel, D. K., Ganguly, K., & Lim, K.-T. (2021b). Isolation and characterization of cellulose nanocrystals from coffee grounds for tissue engineering. *Materials Letters, 287*, Article 129311.

Elder, B., Neupane, R., Tokita, E., Ghosh, U., Hales, S., & Kong, Y. L. (2020). Nanomaterial patterning in 3D printing. *Advanced Materials, 32*, Article 1907142.

Elkhoury, K., Morsink, M., Tahri, Y., Kahn, C., Cleymand, F., Shin, S. R., et al. (2021). Synthesis and characterization of C2C12-laden gelatin methacryloyl (GelMA) from marine and mammalian sources. *International Journal of Biological Macromolecules, 183*, 918–926.

Fourmann, O., Hausmann, M. K., Neels, A., Schubert, M., Nyström, G., Zimmermann, T., et al. (2021). 3D printing of shape-morphing and antibacterial anisotropic nanocellulose hydrogels. *Carbohydrate Polymers, 259*, Article 117716.

Gallagher, Z. J., Fleetwood, S., Kirley, T. L., Shaw, M. A., Mullins, E. S., Ayres, N., et al. (2020). Heparin mimic material derived from cellulose nanocrystals. *Biomacromolecules, 21*, 1103–1111.

Ganguly, K., Jin, H., Dutta, S. D., Patel, D. K., Patil, T. V., & Lim, K.-T. (2022). Magnetic field-assisted aligned patterning in an alginate-silk fibroin/nanocellulose composite for guided wound healing. *Carbohydrate Polymers, 287*, Article 119321.

Ganguly, K., Patel, D. K., Dutta, S. D., & Lim, K.-T. (2021). TEMPO-cellulose nanocrystal-capped gold nanoparticles for colorimetric detection of pathogenic DNA. *ACS Omega, 6*, 12424–12431.

Gao, Q., Niu, X., Shao, L., Zhou, L., Lin, Z., Sun, A., et al. (2019). 3D printing of complex GelMA-based scaffolds with nanoclay. *Biofabrication, 11*, Article 035006.

Garcia-Cruz, M., Postma, A., Frith, J., & Meagher, L. (2021). Printability and bio-functionality of a shear thinning methacrylated xanthan–gelatin composite bioink. *Biofabrication, 13*, Article 035023.

García-Tuñon, E., Barg, S., Franco, J., Bell, R., Eslava, S., D'Elia, E., et al. (2015). Printing in three dimensions with graphene. *Advanced Materials, 27*, 1688–1693.

Garraud, O., Hozzein, W. N., & Badr, G. (2017). Wound healing: time to look for intelligent,'natural'immunological approaches? *BMC Immunology, 18*, 1–8.

Geng, B., Fang, F., Li, P., Xu, S., Pan, D., Zhang, Y., et al. (2021). Surface charge-dependent osteogenic behaviors of edge-functionalized graphene quantum dots. *Chemical Engineering Journal, 417*, Article 128125.

Guo, J., Li, Q., Zhang, R., Li, B., Zhang, J., Yao, L., et al. (2022). Loose pre-cross-linking mediating cellulose self-assembly for 3D printing strong and tough biomimetic scaffolds. *Biomacromolecules, 23*, 877–888.

Habibi, Y., Lucia, L. A., & Rojas, O. J. (2010). Cellulose nanocrystals: Chemistry, self-assembly, and applications. *Chemical Reviews, 110*, 3479–3500.

Heidarian, P., & Kouzani, A. Z. (2023). A self-healing nanocomposite double network bacterial nanocellulose/gelatin hydrogel for three dimensional printing. *Carbohydrate Polymers, 313*, Article 120879.

Highley, C. B., Rodell, C. B., & Burdick, J. A. (2015). Direct 3D printing of shear-thinning hydrogels into self-healing hydrogels. *Advanced Materials, 27*, 5075–5079.

Hong, H., Seo, Y. B., Lee, J. S., Lee, Y. J., Lee, H., Ajiteru, O., et al. (2020). Digital light processing 3D printed silk fibroin hydrogel for cartilage tissue engineering. *Biomaterials, 232*, Article 119679.

Huang, L., Zhu, Z., Wu, D., Gan, W., Zhu, S., Li, W., et al. (2019). Antibacterial poly (ethylene glycol) diacrylate/chitosan hydrogels enhance mechanical adhesiveness and promote skin regeneration. *Carbohydrate Polymers, 225*, Article 115110.

Hyun, H., Park, M. H., Owens, E. A., Wada, H., Henary, M., Handgraaf, H. J., et al. (2015). Structure-inherent targeting of near-infrared fluorophores for parathyroid and thyroid gland imaging. *Nature Medicine, 21*, 192–197.

Jaiswal, A., Rani, S., Singh, G. P., Hassan, M., Nasrin, A., Gomes, V. G., et al. (2021). Additive-free all-carbon composite: A two-photon material system for nanopatterning of fluorescent sub-wavelength structures. *ACS Nano, 15*, 14193–14206.

Jenkins, T. L., & Little, D. (2019). Synthetic scaffolds for musculoskeletal tissue engineering: Cellular responses to fiber parameters. *NPJ Regenerative Medicine, 4*, 15.

Jia, W., Gungor-Ozkerim, P. S., Zhang, Y. S., Yue, K., Zhu, K., Liu, W., et al. (2016). Direct 3D bioprinting of perfusable vascular constructs using a blend bioink. *Biomaterials, 106*, 58–68.

Kim, S. H., Park, J. H., Kwon, J. S., Cho, J. G., Park, K. G., Park, C. H., et al. (2020). NIR fluorescence for monitoring in vivo scaffold degradation along with stem cell tracking in bone tissue engineering. *Biomaterials, 258*, Article 120267.

Kim, S. H., Yeon, Y. K., Lee, J. M., Chao, J. R., Lee, Y. J., Seo, Y. B., et al. (2018). Precisely printable and biocompatible silk fibroin bioink for digital light processing 3D printing. *Nature Communications, 9*, 1–14.

Kong, B., Chen, Y., Liu, R., Liu, X., Liu, C., Shao, Z., et al. (2020). Fiber reinforced GelMA hydrogel to induce the regeneration of corneal stroma. *Nature Communications, 11*, 1–12.

Lee, Y. J., Lee, J. S., Ajiteru, O., Lee, O. J., Lee, J. S., Lee, H., et al. (2022). Biocompatible fluorescent silk fibroin bioink for digital light processing 3D printing. *International Journal of Biological Macromolecules, 213*, 317–327.

Li, V. C.-F., Kuang, X., Mulyadi, A., Hamel, C. M., Deng, Y., & Qi, H. J. (2019). 3D printed cellulose nanocrystal composites through digital light processing. *Cellulose, 26*, 3973–3985.

Liu, H., Zhang, Y., Liu, X., Duan, W., Li, M., Zhou, Q., et al. (2022). Additive manufacturing of nanocellulose/polyborosilazane derived CNFs-SiBCN ceramic metamaterials for ultra-broadband electromagnetic absorption. *Chemical Engineering Journal, 433*, Article 133743.

Liu, J., Li, L., Suo, H., Yan, M., Yin, J., & Fu, J. (2019). 3D printing of biomimetic multi-layered GelMA/nHA scaffold for osteochondral defect repair. *Materials and Design, 171*, Article 107708.

Loebel, C., Rodell, C. B., Chen, M. H., & Burdick, J. A. (2017). Shear-thinning and self-healing hydrogels as injectable therapeutics and for 3D-printing. *Nature Protocols, 12*, 1521–1541.

Luo, H., Cha, R., Li, J., Hao, W., Zhang, Y., & Zhou, F. (2019). Advances in tissue engineering of nanocellulose-based scaffolds: A review. *Carbohydrate Polymers, 224*, Article 115144.

Maturi, M., Pulignani, C., Locatelli, E., Buratti, V. V., Tortorella, S., Sambri, L., et al. (2020). Phosphorescent bio-based resin for digital light processing (DLP) 3D-printing. *Green Chemistry, 22*, 6212–6224.

Meierhofer, R., Dissinger, F., Weigert, F., Jungclaus, J. R., Müller-Caspary, K., Waldvogel, S. R., et al. (2020). Citric acid based carbon dots with amine type stabilizers: pH-specific luminescence and quantum yield characteristics. *The Journal of Physical Chemistry C, 124*, 8894–8904.

Melilli, G., Carmagnola, I., Tonda-Turo, C., Pirri, F., Ciardelli, G., Sangermano, M., et al. (2020). DLP 3D printing meets lignocellulosic biopolymers: Carboxymethyl cellulose inks for 3D biocompatible hydrogels. *Polymers., 12*, 1655.

Mohan, D., Sajab, M. S., Kaco, H., Bakarudin, S. B., & Mohamed Noor, A. A. (2019). 3D printing of UV-curable polyurethane incorporated with surface-grafted nanocellulose. *Nanomaterials, 9*, 1726.

Moniruzzaman, M., Dutta, S. D., Hexiu, J., Ganguly, K., Lim, K.-T., & Kim, J. (2022). Polyphenol derived bioactive carbon quantum dot-incorporated multifunctional hydrogels as an oxidative stress attenuator for antiaging and in vivo wound-healing applications. *Biomaterials Science, 10*, 3527–3539.

Mujtaba, M., Negi, A., King, A. W., Zare, M., & Kuncova-Kallio, J. (2023). Surface modifications of nanocellulose for drug delivery applications; a critical review. *Current Opinion in Biomedical Engineering, 28*, 1–16.

Newman, A. C., Nakatsu, M. N., Chou, W., Gershon, P. D., & Hughes, C. C. (2011). The requirement for fibroblasts in angiogenesis: Fibroblast-derived matrix proteins are essential for endothelial cell lumen formation. *Molecular Biology of the Cell, 22*, 3791–3800.

Nichol, J. W., Koshy, S. T., Bae, H., Hwang, C. M., Yamanlar, S., & Khademhosseini, A. (2010). Cell-laden microengineered gelatin methacrylate hydrogels. *Biomaterials, 31*, 5536–5544.

Ning, L., Mehta, R., Cao, C., Theus, A., Tomov, M., Zhu, N., et al. (2020). Embedded 3D bioprinting of gelatin methacryloyl-based constructs with highly tunable structural fidelity. *ACS Applied Materials & Interfaces, 12*, 44563–44577.

Niu, Q., Gao, K., Lin, Z., & Wu, W. (2013). Amine-capped carbon dots as a nanosensor for sensitive and selective detection of picric acid in aqueous solution via electrostatic interaction. *Analytical Methods, 5*, 6228–6233.

O'Connell, C. D., Zhang, B., Onofrillo, C., Duchi, S., Blanchard, R., Quigley, A., et al. (2018). Tailoring the mechanical properties of gelatin methacryloyl hydrogels through manipulation of the photocrosslinking conditions. *Soft Matter, 14*, 2142–2151.

Ouyang, L., Armstrong, J. P., Lin, Y., Wojciechowski, J. P., Lee-Reeves, C., Hachim, D., et al. (2020). Expanding and optimizing 3D bioprinting capabilities using complementary network bioinks. *Science Advances, 6*, Article eabc5529.

Pal, R., Mamidi, M. K., Das, A. K., & Bhonde, R. (2012). Diverse effects of dimethyl sulfoxide (DMSO) on the differentiation potential of human embryonic stem cells. *Archives of Toxicology, 86*, 651–661.

Park, H. Y., Zoller, S. D., Hegde, V., Sheppard, W., Burke, Z., Blumstein, G., et al. (2021). Comparison of two fluorescent probes in preclinical non-invasive imaging and image-guided debridement surgery of staphylococcal biofilm implant infections. *Scientific Reports, 11*, 1–13.

Patel, D. K., Dutta, S. D., Hexiu, J., Ganguly, K., & Lim, K.-T. (2022). 3D-printable chitosan/silk fibroin/cellulose nanoparticle scaffolds for bone regeneration via M2 macrophage polarization. *Carbohydrate Polymers, 281*, 1–18.

Patel, D. K., Ganguly, K., Dutta, S. D., Patil, T. V., & Lim, K.-T. (2023). Cellulose nanocrystals vs. cellulose nanospheres: A comparative study of cytotoxicity and macrophage polarization potential. *Carbohydrate Polymers, 303*, Article 120464.

Patil, T. V., Patel, D. K., Dutta, S. D., Ganguly, K., Santra, T. S., & Lim, K.-T. (2022). Nanocellulose, a versatile platform: From the delivery of active molecules to tissue engineering applications. *Bioactive Materials, 9*, 566–589.

Quraishi, S., Plappert, S. F., Grießer, T., Gindl-Altmutter, W., & Liebner, F. W. (2019). Chemical versus physical grafting of photoluminescent amino-functional carbon dots onto transparent nematic nanocellulose gels and aerogels. *Cellulose, 26*, 7781–7796.

Sanchez Noriega, J. L., Chartrand, N. A., Valdoz, J. C., Cribbs, C. G., Jacobs, D. A., Poulson, D., et al. (2021). Spatially and optically tailored 3D printing for highly miniaturized and integrated microfluidics. *Nature Communications, 12*, 1–13.

Shin, K., Choi, J. W., Ko, G., Baik, S., Kim, D., Park, O. K., et al. (2017). Multifunctional nanoparticles as a tissue adhesive and an injectable marker for image-guided procedures. *Nature Communications, 8*, 1–12.

Simsek Öz, E., Aydemir, E., & Fışkın, K. (2012). DMSO exhibits similar cytotoxicity effects to thalidomide in mouse breast cancer cells. *Oncology Letters, 3*, 927–929.

Skliutas, E., Lebedevaite, M., Kasetaite, S., Rekštytė, S., Lileikis, S., Ostrauskaite, J., et al. (2020). A bio-based resin for a multi-scale optical 3D printing. *Scientific Reports, 10*, 1–9.

Sultan, S., Abdelhamid, H. N., Zou, X., & Mathew, A. P. (2019). CelloMOF: Nanocellulose enabled 3D printing of metal–organic frameworks. *Advanced Functional Materials, 29*, Article 1805372.

Sultan, S., & Mathew, A. P. (2018). 3D printed scaffolds with gradient porosity based on a cellulose nanocrystal hydrogel. *Nanoscale, 10*, 4421–4431.

Sultan, S., Siqueira, G., Zimmermann, T., & Mathew, A. P. (2017). 3D printing of nano-cellulosic biomaterials for medical applications. *Current Opinion in Biomedical Engineering, 2*, 29–34.

Tran, A., Boott, C. E., & MacLachlan, M. J. (2020). Understanding the self-assembly of cellulose nanocrystals—Toward chiral photonic materials. *Advanced Materials, 32*, Article 1905876.

Wang, Q., Liu, X., Su, M., Shi, Z., & Sun, H. (2014). Study on the interaction characteristics of dexamethasone sodium phosphate with bovine serum albumin by spectroscopic technique. *New Journal of Chemistry, 38*, 4092–4098.

Wang, Z., Abdulla, R., Parker, B., Samanipour, R., Ghosh, S., & Kim, K. (2015). A simple and high-resolution stereolithography-based 3D bioprinting system using visible light crosslinkable bioinks. *Biofabrication, 7*, Article 045009.

Wei, H., Zhang, B., Lei, M., Lu, Z., Liu, J., Guo, B., et al. (2022). Visible-light-mediated nano-biomineralization of customizable tough hydrogels for biomimetic tissue engineering. *ACS Nano, 16*, 4734–4745.

Xie, M., Shi, Y., Zhang, C., Ge, M., Zhang, J., Chen, Z., et al. (2022). In situ 3D bioprinting with bioconcrete bioink. *Nature Communications, 13*, 1–12.

Xu, C., Molino, B. Z., Wang, X., Cheng, F., Xu, W., Molino, P., et al. (2018). 3D printing of nanocellulose hydrogel scaffolds with tunable mechanical strength towards wound healing application. *Journal of Materials Chemistry B, 6*, 7066–7075.

Yang, Y., Xie, X., Yang, Z., Wang, X., Cui, W., Yang, J., et al. (2007). Controlled synthesis and novel solution rheology of hyperbranched poly (urea–urethane)-functionalized multiwalled carbon nanotubes. *Macromolecules, 40*, 5858–5867.

Ye, W., Li, H., Yu, K., Xie, C., Wang, P., Zheng, Y., et al. (2020). 3D printing of gelatin methacrylate-based nerve guidance conduits with multiple channels. *Materials and Design, 192*, Article 108757.

Ying, G. L., Jiang, N., Maharjan, S., Yin, Y. X., Chai, R. R., Cao, X., et al. (2018). Aqueous two-phase emulsion bioink-enabled 3D bioprinting of porous hydrogels. *Advanced Materials, 30*, Article 1805460.

Zhang, Q., Zhang, C., Li, Z., Ge, J., Li, C., Dong, C., et al. (2015b). Nitrogen-doped carbon dots as fluorescent probe for detection of curcumin based on the inner filter effect. *RSC Advances, 5*, 95054–95060.

Zhang, Y., He, Y., Cui, P., Feng, X., Chen, L., Yang, Y., et al. (2015a). Water-soluble, nitrogen-doped fluorescent carbon dots for highly sensitive and selective detection of Hg 2+ in aqueous solution. *RSC Advances, 5*, 40393–40401.

Zhao, F., Repo, E., Song, Y., Yin, D., Hammouda, S. B., Chen, L., et al. (2017). Polyethylenimine-cross-linked cellulose nanocrystals for highly efficient recovery of rare earth elements from water and a mechanism study. *Green Chemistry, 19*, 4816–4828.

Zhao, X., Zhao, Y., Li, M.-D., Za, L., Peng, H., Xie, T., et al. (2021). Efficient 3D printing via photooxidation of ketocoumarin based photopolymerization. *Nature Communications, 12*, 1–8.

Zhou, M., Lee, B. H., Tan, Y. J., & Tan, L. P. (2019). Microbial transglutaminase induced controlled crosslinking of gelatin methacryloyl to tailor rheological properties for 3D printing. *Biofabrication, 11*, Article 025011.

Zhu, W., Ma, X., Gou, M., Mei, D., Zhang, K., & Chen, S. (2016). 3D printing of functional biomaterials for tissue engineering. *Current Opinion in Biotechnology, 40*, 103–112.